



# Integer topological defects organize stresses driving tissue morphogenesis

Pau Guillamat<sup>1,4</sup>, Carles Blanch-Mercader<sup>1,2,4</sup>, Guillaume Pernollet<sup>1</sup>, Karsten Kruse<sup>1,2,3</sup>✉ and Aurélien Roux<sup>1,3</sup>✉

**Tissues acquire function and shape via differentiation and morphogenesis. Both processes are driven by coordinating cellular forces and shapes at the tissue scale, but general principles governing this interplay remain to be discovered. Here we report that self-organization of myoblasts around integer topological defects, namely spirals and asters, suffices to establish complex multicellular architectures. In particular, these arrangements can trigger localized cell differentiation or, alternatively, when differentiation is inhibited, they can drive the growth of swirling protrusions. Both localized differentiation and growth of cellular vortices require specific stress patterns. By analysing the experimental velocity and orientational fields through active gel theory, we show that integer topological defects can generate force gradients that concentrate compressive stresses. We reveal these gradients by assessing spatial changes in nuclear volume and deformations of elastic pillars. We propose integer topological defects as mechanical organizing centres controlling differentiation and morphogenesis.**

In materials, long-range order, robust shapes and patterns can emerge from self-organization phenomena driven by interactions between particles, molecules and atoms, rather than being imposed by external constraints. In active materials, additional energy-consuming processes generate forces that can self-organize to give rise to motion and shape. In tissues, the emergence of shapes arises from the coordination of cellular forces and is referred to as morphogenesis. By analogy, morphogenesis is thus thought to be driven by cellular self-organization. However, because development is under the tight control of genetics, discovering the nature of self-organization mechanisms involved in morphogenesis remains challenging, focusing the efforts of many creative studies<sup>1</sup>.

Akin to elongated molecules in liquid crystals<sup>2</sup>, elongated cells can self-organize into patterns featuring long-range orientational order<sup>3–6</sup>. Orientational fields may present topological defects, regions where the orientational order is ill-defined. Still, defects indicate very specific orientational configurations around their cores<sup>2</sup>. In active systems—driven by internal energy-consuming processes—topological defects entail characteristic flow and stress patterns that depend on the defects' topological strength  $s$ , which indicates the rotation of the orientational field along a path encircling the defect's core<sup>2</sup>. In particular, active half-integer defects ( $s = \pm 1/2$ ) have been thoroughly studied<sup>7–14</sup>. In cell monolayers, their position correlates with cell extrusion<sup>12</sup> or changes in cell density<sup>13</sup>.

Integer topological defects in cell monolayers, such as vortices, spirals or asters ( $s = +1$ ), remain less characterized. Yet, they abound in nature, at cellular, tissue and organismal scales<sup>15</sup>. Astral and spiral cellular patterns have been identified in fibroma<sup>16</sup>, brain tumour<sup>17</sup> and corneal epithelia<sup>18</sup>, where they lead to abnormal cell aggregation in the defect core. Because of their symmetry, integer defects may play essential roles in organizing tissue architecture by stabilizing mechanical patterns. Indeed, integer defects colocalize with the mouth, tentacles and foot of hydra during its development<sup>19</sup>. In vitro, cellular integer defects have been generated by imposing their orientational patterns through cell substrate microstructured<sup>20,21</sup>.

Still, their dynamics and mechanics remain unknown, as well as the mechanisms by which active integer topological defects could directly contribute to remodelling tissues.

## Formation of cellular spirals and asters

Here, we aimed at forming cellular integer topological defects to investigate their role in tissue morphogenesis. To this end, we used C2C12 myoblasts, which feature elongated shapes and can differentiate into myotubes, the precursors of skeletal muscle<sup>22</sup>. Confluent C2C12 cells formed collective alignment with long-range orientational order, referred to as nematic order (Fig. 1a)<sup>5,14,23</sup>. Without confinement, they exhibited topological defects with charges  $s = \pm 1/2$  (Fig. 1a and Methods)<sup>13,14</sup>. The spatial nematic correlation distance,  $\xi_{nn}$ , increased to  $190 \pm 10 \mu\text{m}$  30 h after cell plating (Fig. 1b, Extended Data Fig. 1 and Methods), which set a characteristic length for inter-defect spacing at initial stages (Fig. 1b, inset and Methods).

Inspired by previous studies<sup>14,24–27</sup>, we reasoned that circular confinement of cells below  $\xi_{nn}$  would induce their self-organization around one single defect with  $s = +1$ . C2C12 myoblasts were thus seeded on fibronectin-coated discs (Fig. 1c) with diameters of the order of  $\xi_{nn}$ . After reaching confluence, C2C12 cells self-organized into single-defect configurations featuring well-defined alignment and spontaneous flows. At low density, cells self-organized into spiral configurations with persistent rotation for several hours (Figs. 1d–h, 3–10 h). Further proliferation led to the transformation of spirals into asters (Fig. 1d–h, 10–26 h). In the latter, cells oriented radially from the centre of the disc and ceased to rotate (Fig. 1d–h, 26–33 h and Supplementary Video 1). In active nematic systems, transitions between spirals and asters have been theoretically predicted for changes in activity and elasticity<sup>28</sup>. In our experiments, the spiral-to-aster transition correlated with an increase in cell density (Extended Data Fig. 2a–c) and was reversible, as expanding the confinement after aster formation reestablished the spiral arrangement (Supplementary Video 2). Further work is necessary to unveil the role of density gradients in spiral-to-aster transitions of active

<sup>1</sup>Department of Biochemistry, University of Geneva, Geneva, Switzerland. <sup>2</sup>Department of Theoretical Physics, University of Geneva, Geneva, Switzerland.

<sup>3</sup>NCCR for Chemical Biology, University of Geneva, Geneva, Switzerland. <sup>4</sup>These authors contributed equally: Pau Guillamat, Carles Blanch-Mercader.

✉e-mail: [karsten.kruse@unige.ch](mailto:karsten.kruse@unige.ch); [aurelien.roux@unige.ch](mailto:aurelien.roux@unige.ch)

liquid crystals. Both spiral and aster configurations exhibited accumulation of cells in their centres (Extended Data Fig. 2d) and further proliferation in asters led to the formation of cellular mounds (Fig. 1i,j and Supplementary Video 3). Growth of cellular mounds may also be controlled by nematic order and topological cues. To test this, we characterized the order and dynamics of spirals, asters and mounds.

### Orientation and dynamics of cellular spirals and asters

To stabilize spiral configurations, we inhibited proliferation with Mitomycin-C (Methods). We used OrientationJ<sup>29</sup> to measure locally averaged orientational field from phase-contrast images of Mitomycin-C-stabilized spirals (Fig. 2a, Supplementary Video 4 and Methods). The order parameter  $S$ , which measures the degree of orientational order, was minimal at the discs centre and increased towards their boundaries (Fig. 2b,c and Methods). The angle  $\psi$  between local orientation and the radial direction was  $79 \pm 5^\circ$  ( $N=12$ , Fig. 2d and Methods). The orientational field extracted from fluorescence images of spirals labelled with SiR-actin (Methods) showed comparable  $\psi$  distribution, nematic order profile, and rotation dynamics (Fig. 2a, inset, Extended Data Fig. 3 and Supplementary Video 5), supporting that the orientational field measured from phase-contrast images is determined by actin structures.

The average velocity field was extracted from phase-contrast videos of spirals with particle image velocimetry<sup>30</sup> (PIV) (Methods). The velocity was maximal near boundaries at  $27 \pm 7 \mu\text{m h}^{-1}$ , dominantly azimuthal, as was the direction of cell migration (Fig. 2a), with non-vanishing radial component (Fig. 2b,c,  $N=12$ ). The angle between the local orientation and the velocity was not null,  $\beta = 23 \pm 5^\circ$  (Fig. 2d, inset,  $N=12$ ), similar to monolayers of elongated cells confined to stripes<sup>23</sup> or externally sheared liquid crystal slabs<sup>2</sup>. When inhibiting myosin-driven contractility with either Blebbistatin or the ROCK inhibitor Y-27632 (Methods), we observed a notable impact on the spirals' arrangement. Although rotation persisted,  $\psi$  decreased to  $60 \pm 5^\circ$  with Blebbistatin ( $N=21$ ) and to  $63 \pm 4^\circ$  with Y-27632 ( $N=20$ ). Radial velocity substantially increased (Extended Data Fig. 4). The decrease of  $\psi$  in spirals as a result of partial inhibition of contractility is consistent with theory predicting transitions from spirals to asters driven by a decrease in activity<sup>28</sup>.

Above roughly  $2.5 \times 10^{-3} \text{ cells } \mu\text{m}^{-2}$  ( $N=13$ ), C2C12 cells formed stable aster arrangements (Fig. 2e and Supplementary Video 6). Like in spirals,  $S$  increased towards the boundaries, but both orientation and velocity were strictly radial (Fig. 2e–h, Extended Data Fig. 5). Fluorescence images of SiR-actin-labelled asters revealed a radial disposition of actin fibres (Fig. 2e, inset, Extended Data Fig. 5 and Supplementary Video 7). The radial velocity component (Fig. 2f,g) was comparable to that in spirals (Fig. 2b,c). However, cells at the periphery remained almost immobile (Fig. 2e and Supplementary Video 6). We thus suspected

that the radial velocity originated from actin flows. PIV from images of SiR-actin-labelled asters revealed net inward radial velocities similar to those observed by phase-contrast microscopy (Fig. 2e–h, Extended Data Fig. 5 and Supplementary Video 7). These observations support that both the orientation and the velocity fields in asters are related to the morphology and dynamics of actin structures.

To study how cellular mounds formed, we characterized their orientation in three dimensions. SiR-actin-labelled mounds were imaged with confocal z-stacks for several hours (Fig. 3a and Methods). The three-dimensional (3D) orientation of actin fibres was averaged in the azimuthal direction revealing a peripheral order that was lost in the centres of mounds (Fig. 3b and Methods). To evaluate the orientation field in mounds, radial distributions for the elevation angle  $\phi$  and the azimuthal angle  $\varphi$  were extracted at different heights (Fig. 3c,d). The elevation angle  $\phi$ , between vertical axis and cells' orientation, was roughly  $0^\circ$  at the top of the mound, whereas an oblique component,  $\phi$  roughly equal to  $45^\circ$ , appeared at the bottom (Fig. 3c).  $\varphi$  exhibited a bimodal distribution with peaks around  $0^\circ$  and  $90^\circ$ . Below  $10 \mu\text{m}$ ,  $\varphi$  was roughly  $0^\circ$ , whereas above  $10 \mu\text{m}$ ,  $\varphi$  roughly equalled  $90^\circ$  (Fig. 3d). Therefore, cells formed asters at the bottom of mounds and spirals at their top, featuring radial and rotational flows, respectively (Supplementary Video 8 and Methods). This aster-to-spiral transition is consistent with the one shown in Fig. 1d as cell density decreased from bottom-to-top (Fig. 3e,f and Methods).

### Force field around integer topological defects in mounds

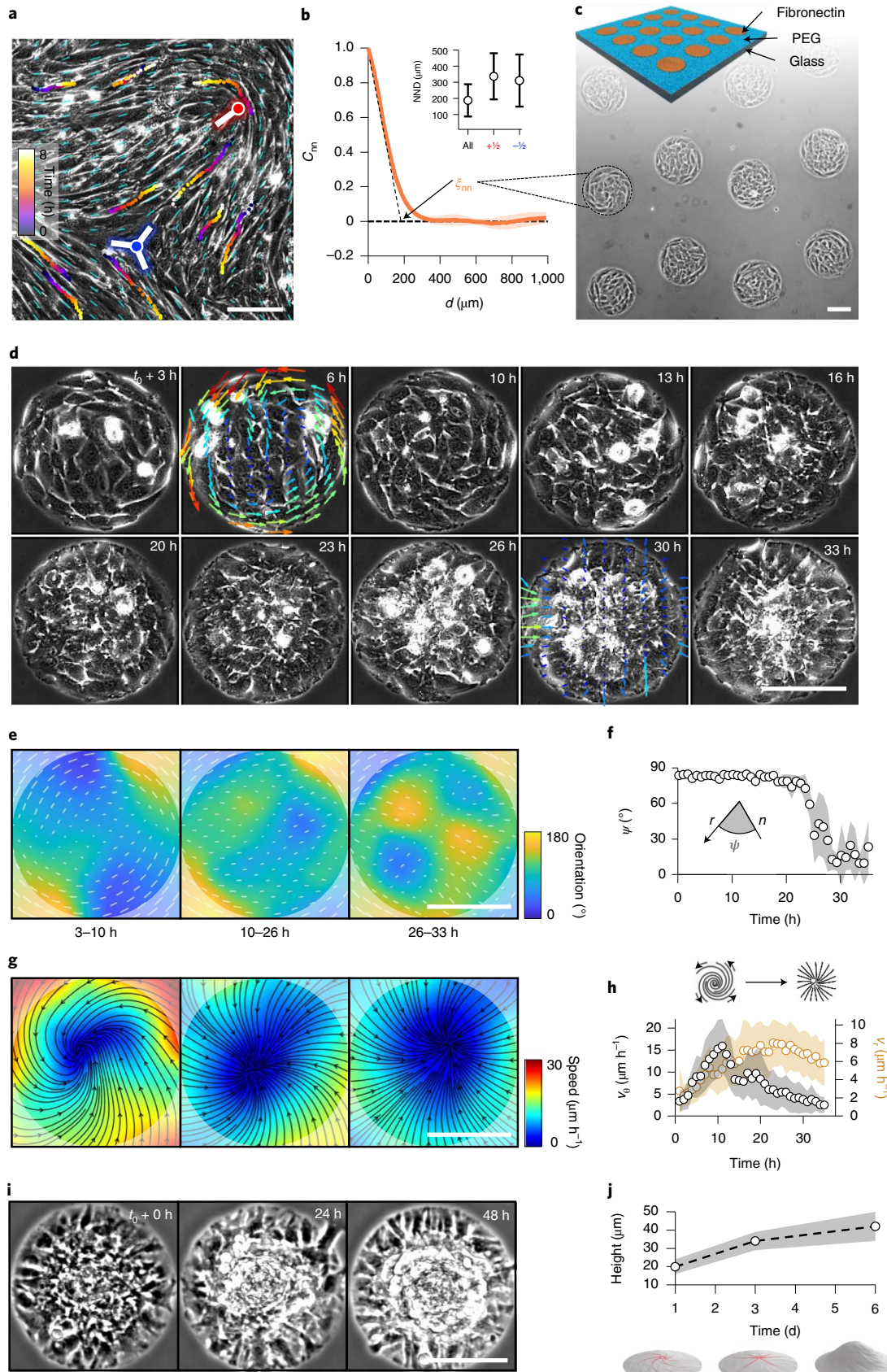
To explain the specific stress fields corresponding to spirals and asters, we developed a theoretical description of a two-dimensional (2D) active polar fluid. The cell monolayer state is characterized by the cell velocity field  $v$ , the cell number density field  $\rho$  and the cell polarization field  $p$ . In absence of active processes, the dynamics of the cell monolayer is governed by the hydrodynamics of passive liquid crystals<sup>2</sup>. To describe our system, we consider contributions of two active processes: the directional motility of cells via traction forces and the cytoskeleton rearrangement via active stresses. This theory is summarized in the Supplementary Note 1 and described in detail elsewhere<sup>31,32</sup>.

Previous studies showed that bidimensional rotational flows can arise either from traction forces of active particles<sup>24,33–35</sup> or from gradients in anisotropic active stresses<sup>28,36</sup>. To constrain the values of our parameters, we fitted our theoretical results to the experimental azimuthal velocity and orientational order profiles of spirals with radii of 50, 100 and 150  $\mu\text{m}$  (Fig. 4a–c and Supplementary Note 2). Solutions that exhibited cell accumulation in the confinement centre, as observed experimentally (Figs. 1i,j and 4d,e and Extended Data Fig. 2d), implied that the contribution from traction forces cannot dominate over that from active stresses<sup>31,32</sup>. In these solutions, compressive stress increased with the cell density (Fig. 4f,g and Methods).

**Fig. 1 | Myoblasts arrange into integer topological defects on circular micropatterns.** **a**, Phase-contrast image of a confluent monolayer of myoblasts. Cyan dashes indicate the local orientational field. Positions of half-integer topological defects are shown (blue dot,  $s = -\frac{1}{2}$ ; red dot,  $s = +\frac{1}{2}$ ). Trajectories of single cells are depicted with colour gradients. Colour map represents time. **b**, Spatial autocorrelation function  $C_{nn}$  of the orientational field.  $\xi_{nn}$  is the nematic correlation length. Inset: nearest-neighbour distance (NND) between half-integer,  $+\frac{1}{2}$  and  $-\frac{1}{2}$  topological defects. **c**, Scheme of the micropatterned surface and corresponding phase-contrast image with confined myoblasts in circular domains of radius  $r = 100 \mu\text{m}$ . **d**, Time series of a single myoblast disc ( $r = 100 \mu\text{m}$ ).  $t = t_0$  at the onset of confluence. For clarity, velocity fields are only shown for 6 and 30 h. The colour map depicts the local average speed. Colour bar in **g**. **e**, Time-averaged orientational field calculated from **d** ( $N=1$ ). Vectors and colour map depict local cellular orientation with respect to the  $x$  axis. The amplitude of the vectors corresponds to the coherency (Methods). **f**, Mean value of angle  $\psi$  between the local orientation and the radial direction over time ( $N=12$ ). **g**, Time-averaged flow field calculated from **d** ( $N=1$ ). Flow directions are shown as black streamlines. The colour map depicts the local average speed. In **e** and **g**, semitransparent areas enclose a region corresponding to a circle with a radius of  $100 \mu\text{m}$ . **h**, Absolute values of the average azimuthal ( $v_\theta$ ) and radial ( $v_r$ ) velocities over time ( $N=12$ ). **i**, Time series of myoblast asters ( $r = 100 \mu\text{m}$ ) forming cellular mounds.  $t = t_0$  at the onset of mound formation. **j**, Average height of myoblast assemblies with time ( $N=17, 10, 16$ , for mounds at 1, 3 and 6 days after the onset of confluence, respectively). In **b** and **j**, data are presented as mean  $\pm$  s.d. In **f** and **h**, data are presented as mean  $\pm$  s.e.m. Scale bars,  $100 \mu\text{m}$ .

To test our theory, we obtained stress gradients within mounds from volume changes of cell nuclei<sup>37,38</sup> (Methods) and found them to match our theoretical results (Fig. 4g). In the centre of the

mounds, both density and compressive stresses increased with time (Fig. 4e,g). We found that in the absence of orientational order, the experimental density and stress profiles cannot be



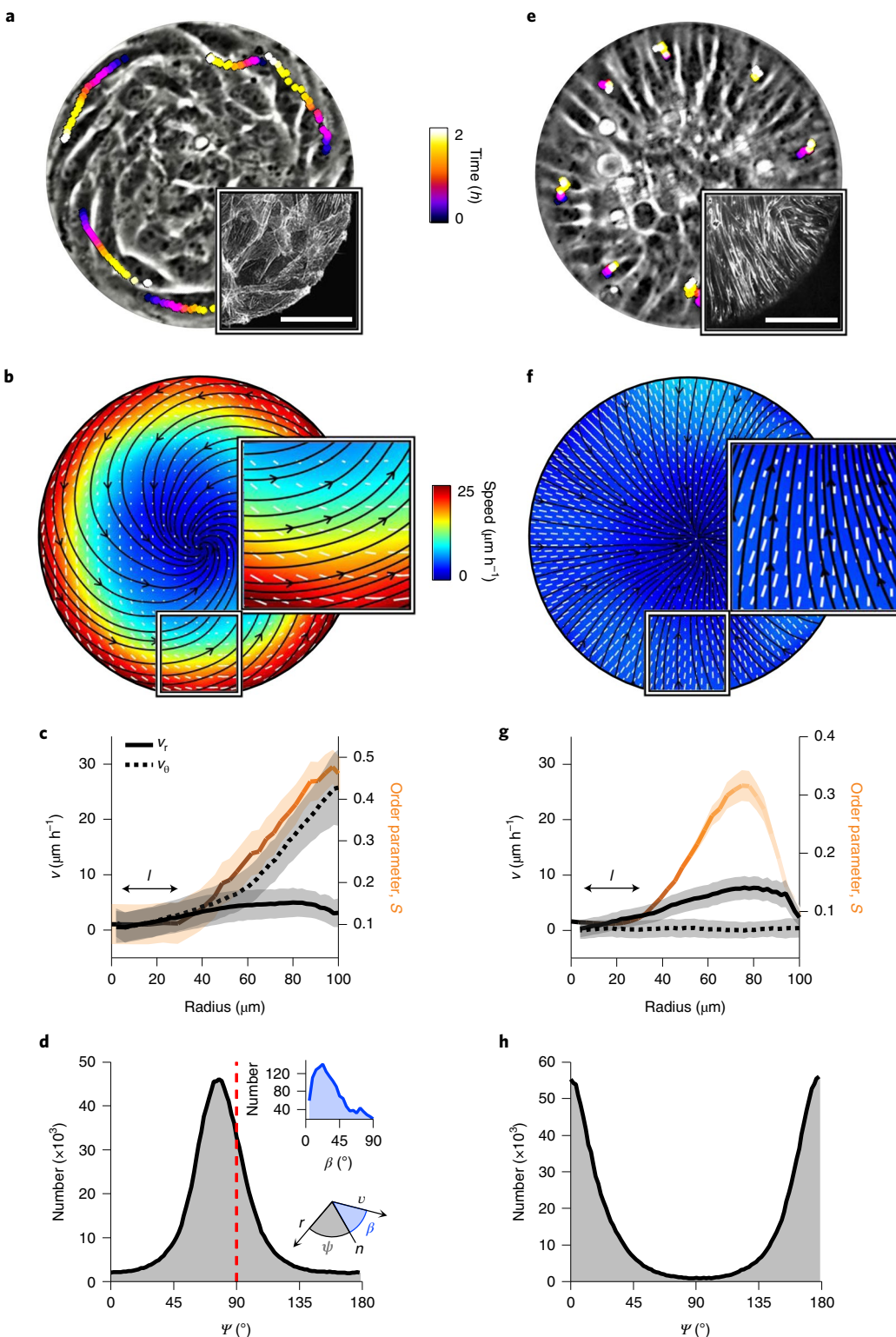


**Fig. 2 | Cellular spiral and aster configurations.** **a,e**, Phase-contrast images of spiral (**a**) and aster (**e**) arrangements ( $r=100\text{ }\mu\text{m}$ ). Trajectories of single cells are depicted with colour gradients. Colour map represents time. Insets: confocal images of the actin fibres at the base of a spiral and an aster, respectively. Actin was stained with SiR-actin. Scale bars,  $50\text{ }\mu\text{m}$ . **b,f**, Average velocity and orientation fields for spirals (**b**) and asters (**f**). Streamlines indicate the direction of the cellular flows. Colour map represents average speed. White lines indicate local cellular orientation; their length corresponds to the coherency (Methods). **c,g**, Radial profiles of the average azimuthal ( $v_\theta$ , dashed black) and radial velocity ( $v_r$ , solid black) components in absolute values, and the profiles of  $S$  (orange) for spirals (**c**) and asters (**g**).  $l$  is the size of the defect core. Data are presented as mean  $\pm$  s.e.m. **d,h**, Distribution of the angle  $\psi$  for spirals (**d**) and asters (**h**). Insets in **d** show the distribution of the angle  $\beta$  between the velocity and cell orientation calculated from **b**, and depict the angles  $\psi$  and  $\beta$ . Panels **b-d** correspond to spirals ( $N=12$ ), and parts **f-h** correspond to asters ( $N=43$ ).

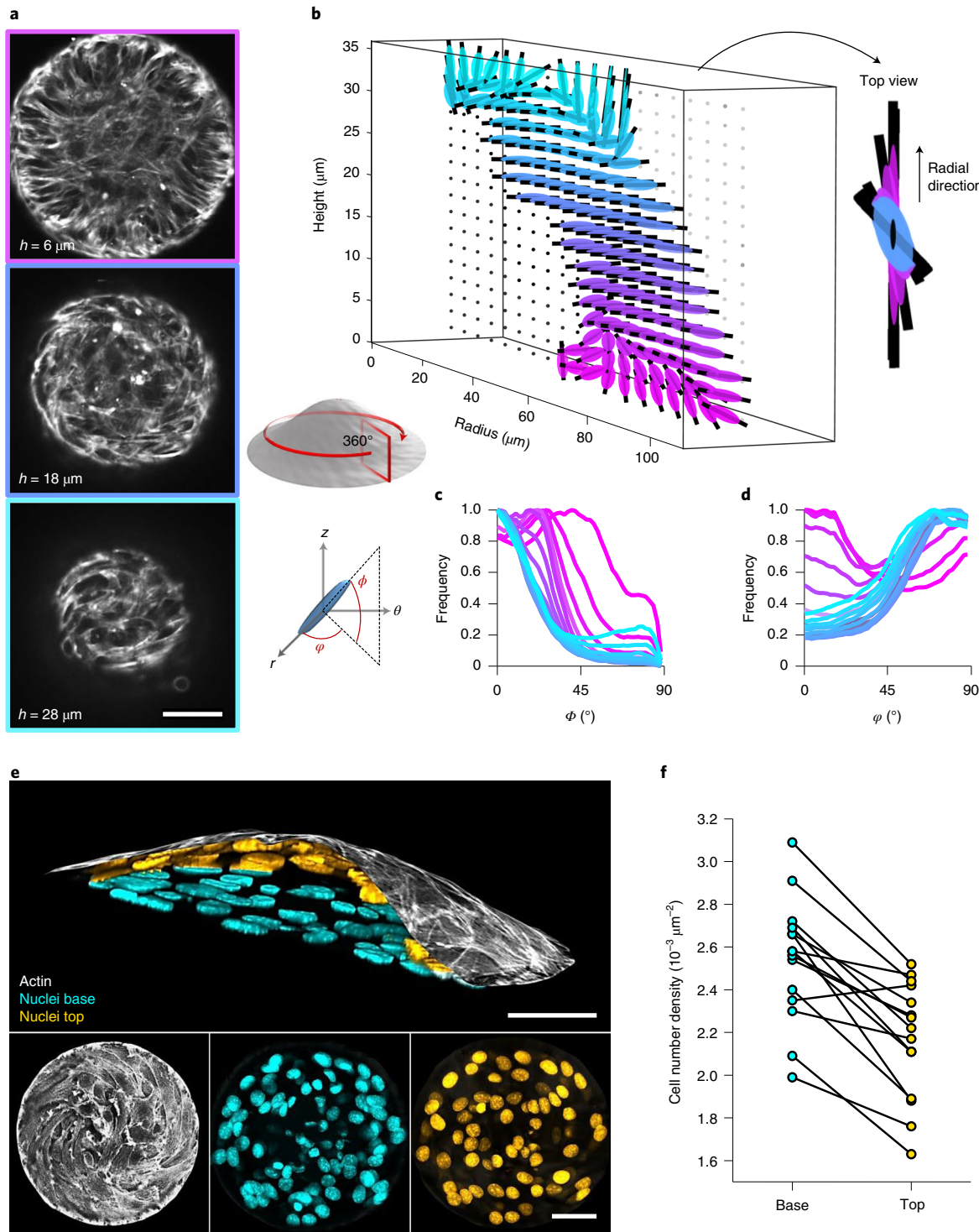


**Fig. 3 | Minimal nematic cellular mounds.** **a**, Confocal images of an actin-labelled cell mound at different heights ( $h$ ). **b**, Three-dimensional orientational field averaged in the azimuthal direction and in time (schematic below), showing on the right a top view at a radial distance of  $80 \mu\text{m}$ . **c,d**, Histograms of the elevation ( $\phi$ ) (**c**) and azimuth ( $\varphi$ ) (**d**) angles (schematic on the left) for different heights. **e**, Vertical section of a cellular mound (top): actin on the top surface (white) and nuclei from the base (cyan) and top (orange) surfaces. Bottom panels show the corresponding vertical projections. **f**, Cell number density for the base and top surfaces for different cellular mounds ( $N=15$ ). Actin was stained with SiR-actin. Nuclei were stained with Hoechst 33342. Scale bars,  $50 \mu\text{m}$ .

reproduced by the theory (Supplementary Note 3). Additionally, our theoretical description suggests that when active anisotropic stresses dominate, then the compressive stress in asters exceeds that in spirals (Supplementary Note 4). Consequently, in mounds, the aster-to-spiral transition as a function of height could be

associated with a vertical stress gradient, promoting growth by driving an upward cellular flow.

To further assess the stresses generated in mounds, we seeded myoblasts on circular fibronectin rings enclosing non-adhesive fluorescent micropillars with an elastic modulus  $E$  of roughly  $4 \text{kPa}$

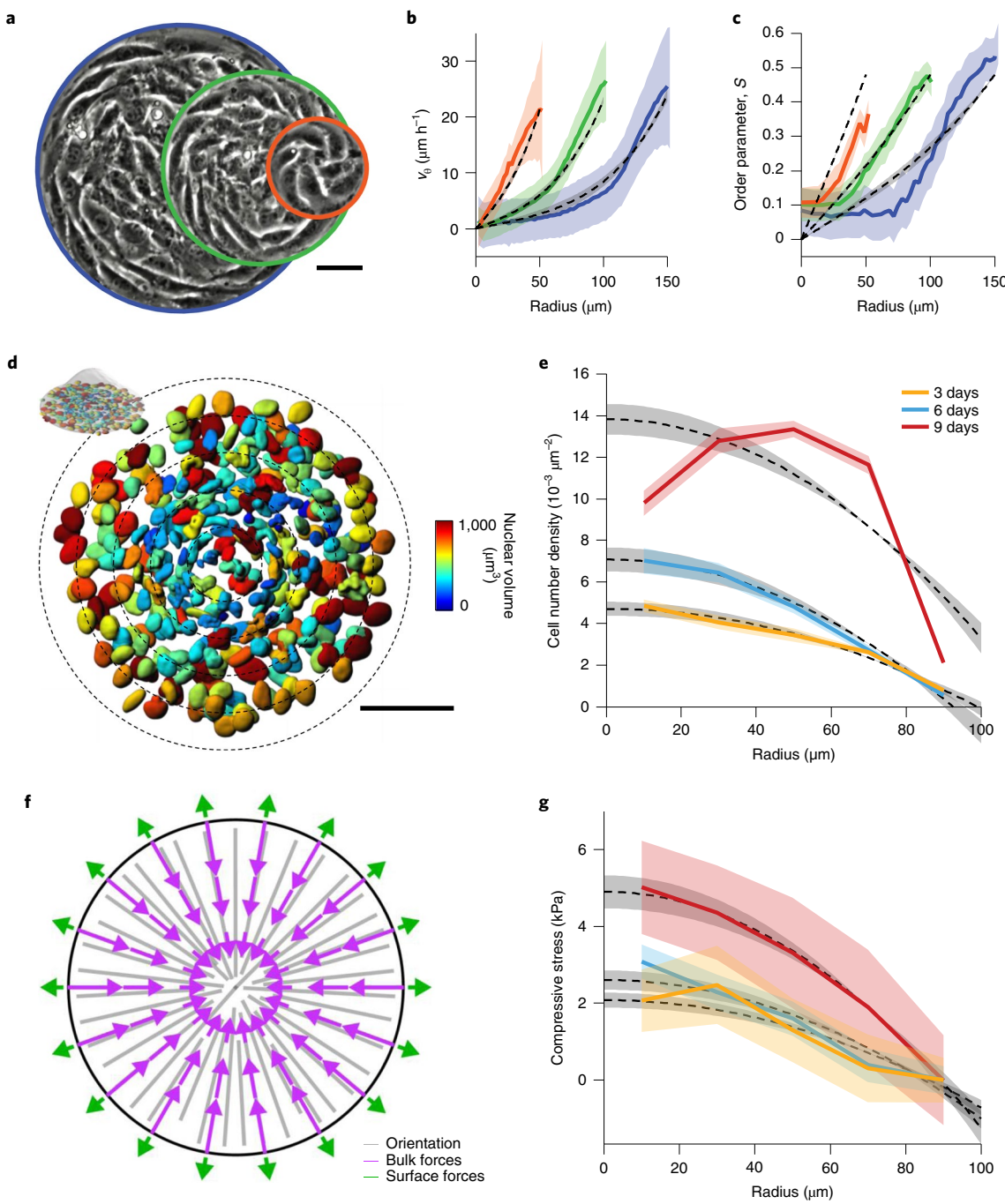


**Fig. 4 | Integer topological defects concentrate active stress.** **a**, Phase-contrast images of spiral defects in cell monolayers confined to circular domains of radii  $r=50$  (orange), 100 (green) and 150  $\mu\text{m}$  (blue). **b,c**, Radial profiles of the average azimuthal velocity  $v_\theta$  (**b**) and the orientational order parameter  $S$  (**c**) ( $N=11$ , 12 and 15 for  $r=50, 100$  and 150  $\mu\text{m}$ , respectively) and theoretical fits (dashed grey lines). **d**, 3D rendering of nuclei at the base of a 9-day-old cellular mound ( $r=100 \mu\text{m}$ ). Colour map indicates nuclear volume. Nuclei were stained with Hoechst 33342. Scale bars, 50  $\mu\text{m}$ . **e**, Radial cell density profiles for aster bases of 3-, 6- and 9-day-old cellular mounds and theoretical fits (dashed grey lines). **f**, Steady-state active forces in asters. **g**, Compressive stress profiles extracted from nuclear deformations for aster bases of 3-, 6- and 9-day-old cellular mounds ( $N=9, 40$  and 10 for 3-, 6- and 9-day-old cellular mounds, respectively) and theoretical fits (dashed grey lines). In experimental plots, data are presented as mean  $\pm$  s.e.m. In theoretical plots, shaded areas correspond to the uncertainty of the fitting method (Supplementary Note 2). For more details on the theoretical curves and fitting analyses, see also Supplementary Note 2.

(Fig. 5a, Supplementary Note 5 and Methods). After confluence on the adhesive fibronectin patterns, myoblasts accommodated around the pillars and compressed them (Fig. 5b,c, Extended Data Figs. 6 and 7a,b and Supplementary Video 9). This compression was compatible with the stresses inferred from nuclear volume changes (Fig. 4g). We determined the stresses on the pillars from their elastic

deformations (Methods). After roughly 30 h, the stresses exerted by cellular mounds saturated at maximum values between 1–4 kPa and were smaller for larger pillar radii (Extended Data Fig. 7c–e).

Actomyosin cables and multicellular rings have been shown to play an important role in gap closure<sup>39</sup> and in the generation of compressive stresses<sup>40</sup>. We performed several experiments to confirm

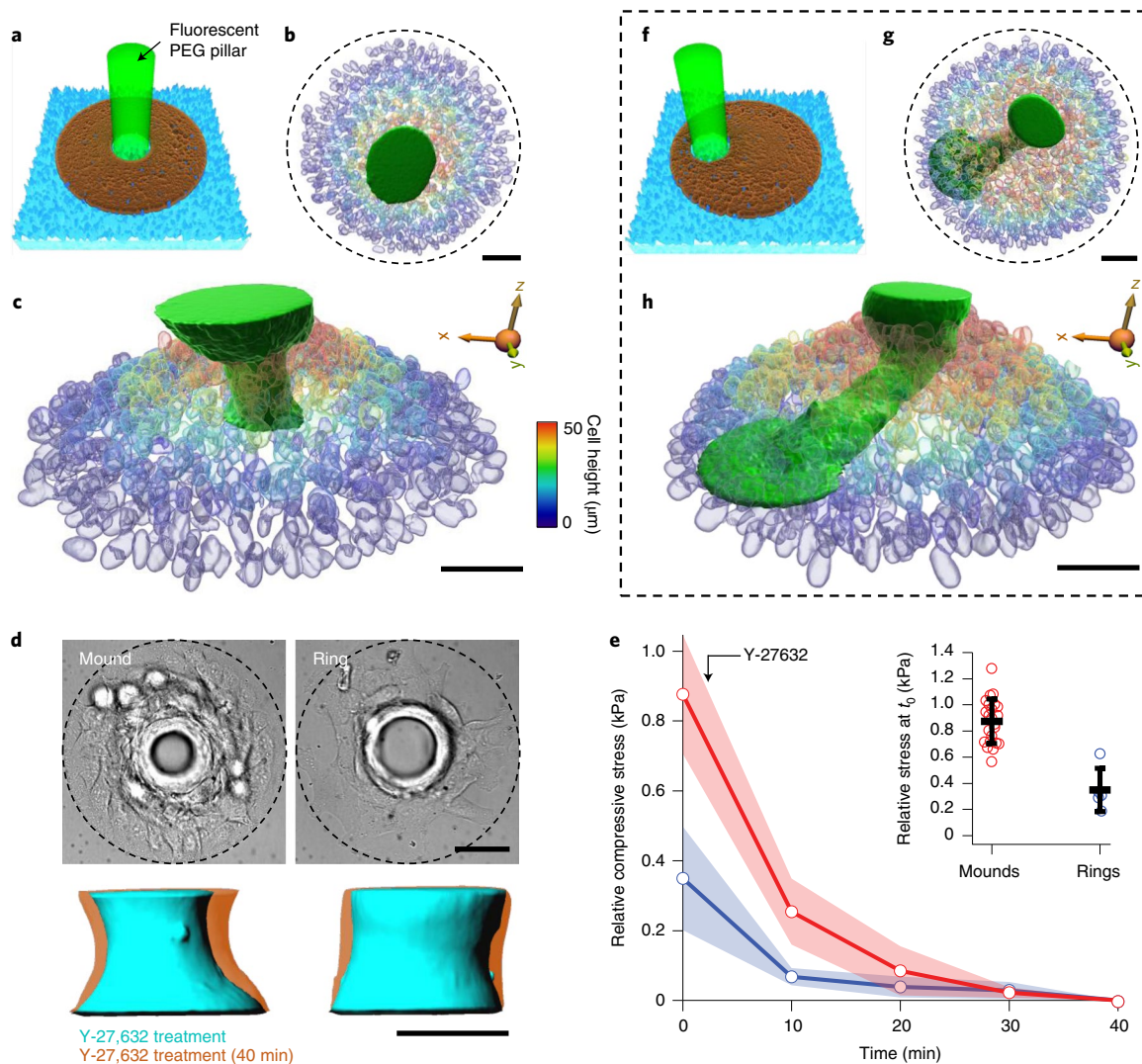


**Fig. 5 | Soft pillars in compressive cellular mounds.** **a**, Scheme of a pillar deformation experiment. A fluorescent-PEG pillar (green) is surrounded by a cell-adhesive fibronectin pattern (brown), enclosed by non-adhesive PEG (cyan). **b**, Top view of a 3D rendering from confocal stacks showing the nuclei in a mound surrounding and compressing a PEG pillar. **c**, Side view of the experiment in **b**. Colour map indicates height of cells in **b** and **c**. **d**, Top: brightfield (differential interference contrast) images of a cellular mound (left) and a cellular ring (right) around a pillar; bottom: 3D renderings of pillars before (cyan) and 40 min after (orange) Y-27632 treatment corresponding to top panels. **e**, For cellular mounds (red) and cellular rings (blue), relative compressive stress in time after application of Y-27632, which was added immediately after time = 0. Data are presented as mean  $\pm$  s.d. Inset shows the difference in compressive stress between the times of 0 and 40 min in cellular mounds and cellular rings. **f-h**, As **a-c** but for an experiment in which the pillar is off centre. Nuclei were stained with Hoechst 33342. Scale bars, 50  $\mu$ m.

that most of the stresses contributing to pillar compression in mounds were independent of actin or multicellular rings (Fig. 5d,e and Supplementary Note 6).

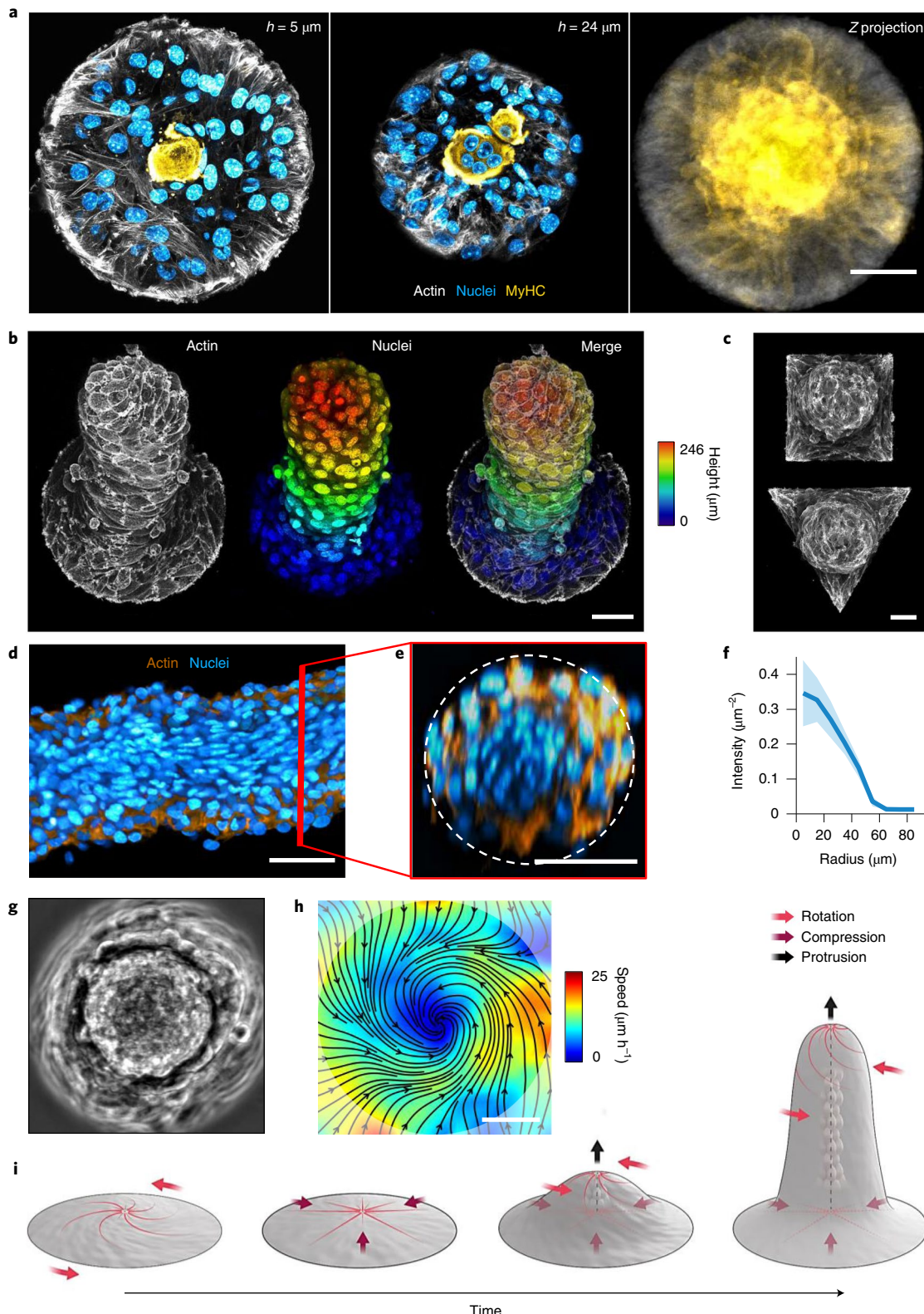
Finally, to better evidence stress gradients, we positioned pillars off centre (Fig. 5f). After the formation of mounds, these pillars appeared strongly bent towards the confinement centres (Fig. 5g,h and Extended Data Fig. 7h-i). These deformations are qualitatively captured by the theory of elastic rods subjected to stress gradients as generated by our cellular mounds (Supplementary Note 7).

### Integer topological defects in mounds localize differentiation of myoblasts

Further evolution of mounds depended on whether myoblasts could differentiate or not. In the first case, myoblasts differentiated and fused into globular multinucleated structures that expressed the muscle-specific protein myosin heavy chain (MyHC) (Fig. 6a and Extended Data Fig. 8a). These differentiated syncytia localized

preferentially at the centre of mounds, suggesting that the compressive stress patterns generated by integer defects in mounds can localize differentiation (Fig. 6a, right panel and Extended Data Fig. 8b). When differentiation was biochemically induced by serum deprivation, myotubes exhibited a broader spatial distribution in spite of a similar distribution of mechanical stress (Extended Data Fig. 8c-e and Methods). Besides, in this case, myotubes mainly presented canonical elongated morphologies (Extended Data Fig. 8c). These findings indicate that biochemical signalling is a stronger trigger of differentiation than mechanical cues. However, it does not lead to spatially patterned differentiation and thus further supports the importance of mechanics for localizing differentiation.

**Cellular protrusions organized by integer topological defects**  
During morphogenesis, however, proliferating cells usually do not differentiate<sup>41</sup>. Accordingly, we sought to inhibit differentiation to promote further proliferation of mounds and study their 3D



shape evolution. As previously observed<sup>42</sup>, C2C12 cells cultured at high-passage numbers were unable to differentiate (Extended Data Fig. 9a). In this case, cellular mounds grew further in height, forming cylindrical protrusions up to hundreds of micrometres (Fig. 6b and Extended Data Figs. 9b and 10a).

The stability of these large multicellular structures was strictly dependent on confinement as degradation of the surrounding

non-adhesive coating induced the protrusions to collapse (Supplementary Video 10). Other confinement geometries, namely squares and triangles, topologically equivalent to a disc, also led to the growth of cylindrical protrusions (Fig. 6c). After 6 days, larger confinement sizes also led to the formation of mounds, which were flatter for bigger confinements and organized around integer topological defects (Extended Data Fig. 10b-d). Furthermore, in our

**Fig. 6 | Topological defects organize differentiation and morphogenesis in 3D nematic tissues.** **a**, Confocal images at different heights ( $h$ ) showing the preferential position for MyHC expression. Confinement radius  $r=100\text{ }\mu\text{m}$ . Left panel corresponds to the first layer of cells. Centre panel corresponds to the midplane, displaying a multinucleated myotube-like structure. Right panel shows the projection of MyHC intensity ( $N=43$ ). **b**,  $z$  projection of a 12-day-old cellular protrusion. Colour map indicates height. **c**,  $z$  projection of 6-day-old protrusions that were grown on patterns with the same area but different geometries. **d**, Cross-section of a tilted protrusion along the protrusion long axis, which goes from left to right in the panel. **e**, Cross-section of the tilted protrusion perpendicular to the protrusion long axis and along the red line in **d**. Dashed line corresponds to a circle of radius  $r=50\text{ }\mu\text{m}$ . **f**, Radial profile of fluorescence intensity per unit area from the nuclei average along the azimuthal and the main protrusion axis directions for the protrusion in **d**. Sections were centred before extracting the intensity profile ( $N=191$  sections). Data are presented as mean  $\pm$  s.d. **g,h**, Phase-contrast image of top view of a 9-day-old protrusion (**g**) and corresponding average velocity field (**h**). Streamlines indicate the direction of the cellular flows. Colour map represents average speed. **i**, Scheme of the time evolution of cellular nematic architectures from two to three dimensions. Actin was stained with SiR-actin. MyHC was stained with the Myosin-4 Monoclonal Antibody conjugated with Alexa Fluor 488. Nuclei were stained with Hoechst 33342. Scale bars,  $50\text{ }\mu\text{m}$ .

theory, by forcing integer topological defects in the absence of confinement, we obtained qualitatively similar stress profiles around the defects (Supplementary Note 8). Altogether, this indicates that, in these cellular arrangements, topological defects and the specific orientational order around them play the prime role in the formation of protrusions.

The density of nuclei was larger in the core of protrusions than at the periphery (Fig. 6d–f), similar to the density patterns in the confined monolayers (Fig. 4e). This suggests that cells at the core were subjected to compressive stresses. Consistent with this idea, nuclei in the core of these protrusions often displayed highly anisometric shapes, elongated along the protrusions' long axis (Fig. 6d). These compressive stresses could be generated by the specific organization of cells in the protrusions.

We observed collective rotation around the protrusions' axis (Fig. 6g–i and Supplementary Video 10). This feature indicates that cells were organized as a 3D vortex, which is also supported by the azimuthal orientation of cells in the external layer of the protrusions (Fig. 6b and Extended Data Fig. 9b) and the twisted cylindrical shapes exhibited by some protrusions after 14 days (Extended Data Fig. 9b). We concluded that minimal cellular mounds based on asters and spirals can evolve into cylindrical vortices, the shape and dynamics of which are dominated by the interplay between nematic order and topological constraints (Fig. 6i).

In summary, our findings show how integer topological defects control the self-organization of myoblast monolayers, localizing differentiation and steering 3D morphogenesis through mechanics. We foresee that integer topological defects could mechanically control multiple cell fate decisions and morphogenetic movements during development.

## Online content

Any methods, additional references, Nature Research reporting summaries, source data, extended data, supplementary information, acknowledgements, peer review information; details of author contributions and competing interests; and statements of data and code availability are available at <https://doi.org/10.1038/s41563-022-01194-5>.

Received: 4 July 2020; Accepted: 3 January 2022;

Published online: 10 February 2022

## References

1. Stooke-Vaughan, G. A. & Campàs, O. Physical control of tissue morphogenesis across scales. *Curr. Opin. Genet. Dev.* **51**, 111–119 (2018).
2. de Gennes, P. G. & Prost, J. *The Physics of Liquid Crystals* (Clarendon Press, 1995).
3. Kemkemer, R., Kling, D., Kaufmann, D. & Gruler, H. Elastic properties of nematoid arrangements formed by amoeboid cells. *Eur. Phys. J. E* **1**, 215 (2000).
4. Junkin, M., Leung, S. L., Whitman, S., Gregorio, C. C. & Wong, P. K. Cellular self-organization by autocatalytic alignment feedback. *J. Cell Sci.* **124**, 4213–4220 (2011).
5. Duclos, G., Garcia, S., Yevick, H. G. & Silberzan, P. Perfect nematic order in confined monolayers of spindle-shaped cells. *Soft Matter* **10**, 2346–2353 (2014).
6. Morales-Navarrete, H. et al. Liquid-crystal organization of liver tissue. *eLife* **8**, e44860 (2019).
7. Sanchez, T., Chen, D. T. N., DeCamp, S. J., Heymann, M. & Dogic, Z. Spontaneous motion in hierarchically assembled active matter. *Nature* **491**, 431–434 (2012).
8. Keber, F. C. et al. Topology and dynamics of active nematic vesicles. *Science* **345**, 1135–1139 (2014).
9. Kumar, N., Zhang, R., de Pablo, J. J. & Gardel, M. L. Tunable structure and dynamics of active liquid crystals. *Sci. Adv.* **4**, eaat7779 (2018).
10. Thampli, S. P., Golestanian, R. & Yeomans, J. M. Instabilities and topological defects in active nematics. *Europhys. Lett.* **105**, 18001 (2014).
11. Giomi, L. Geometry and topology of turbulence in active nematics. *Phys. Rev. E* **91**, 031003 (2015).
12. Saw, T. B. et al. Topological defects in epithelia govern cell death and extrusion. *Nature* **544**, 212–216 (2017).
13. Kawaguchi, K., Kageyama, R. & Sano, M. Topological defects control collective dynamics in neural progenitor cell cultures. *Nature* **545**, 327–331 (2017).
14. Duclos, G., Erlenkamper, C., Joanny, J.-F. & Silberzan, P. Topological defects in confined populations of spindle-shaped cells. *Nat. Phys.* **13**, 58–62 (2017).
15. Thompson, D. W. *On Growth and Form* (Cambridge Univ. Press, 1942).
16. Mandal, S., Mahajan, D., Roy, S., Singh, M. & Khurana, N. Fibroma with minor sex cord elements: an incidental finding in a normal sized ovary—a case report with literature review. *Diagn. Pathol.* **2**, 46 (2007).
17. Kepes, J. J. Cellular whorls in brain tumors other than meningiomas. *Cancer* **37**, 2232–2237 (1976).
18. Dua, H. S. et al. Vortex or whorl formation of cultured human corneal epithelial cells induced by magnetic fields. *Eye* **10**, 447–450 (1996).
19. Maroudas-Sacks, Y. et al. Topological defects in the nematic order of actin fibres as organization centres of Hydra morphogenesis. *Nat. Phys.* **17**, 251–259 (2021).
20. Turiv, T. et al. Topology control of human fibroblast cells monolayer by liquid crystal elastomer. *Sci. Adv.* **6**, eaaz6485 (2020).
21. Endresen, K. D., Kim, M., Pittman, M., Chen, Y. & Serra, F. Topological defects of integer charge in cell monolayers. *Soft Matter* **17**, 5878–5887 (2021).
22. Yaffe, D. & Feldman, M. The formation of hybrid multinucleated muscle fibers from myoblasts of different genetic origin. *Dev. Biol.* **11**, 300–317 (1965).
23. Duclos, G. et al. Spontaneous shear flow in confined cellular nematics. *Nat. Phys.* **14**, 728–732 (2018).
24. Wioland, H., Woodhouse, F. G., Dunkel, J., Kessler, J. O. & Goldstein, R. E. Confinement stabilizes a bacterial suspension into a spiral vortex. *Phys. Rev. Lett.* **110**, 268102 (2013).
25. Guillamat, P., Ignés-Mullol, J. & Sagués, F. Taming active turbulence with patterned soft interfaces. *Nat. Commun.* **8**, 564 (2017).
26. Opathalage, A. et al. Self-organized dynamics and the transition to turbulence of confined active nematics. *Proc. Natl Acad. Sci. USA* **116**, 4788–4797 (2019).
27. Jalal, S. et al. Actin cytoskeleton self-organization in single epithelial cells and fibroblasts under isotropic confinement. *J. Cell Sci.* **132**, jcs220780 (2019).
28. Kruse, K., Joanny, J. F., Jülicher, F., Prost, J. & Sekimoto, K. Aster, vortices, and rotating spirals in active gels of polar filaments. *Phys. Rev. Lett.* **92**, 078101 (2004).
29. Püsöki, Z., Storath, M., Sage, D. & Unser, M. in *Focus on Bio-Image Informatics* (eds De Vos, W. H., Munck, S. & Timmermans, J.-P.) 69–93 (Springer, 2016).
30. Tseng, Q. et al. Spatial organization of the extracellular matrix regulates cell-cell junction positioning. *Proc. Natl Acad. Sci. USA* **109**, 1506–1511 (2012).

31. Blanch-Mercader, C., Guillamat, P., Roux, A. & Kruse, K. Quantifying material properties of cell monolayers by analyzing integer topological defects. *Phys. Rev. Lett.* **126**, 028101 (2021).
32. Blanch-Mercader, C., Guillamat, P., Roux, A. & Kruse, K. Integer topological defects of cell monolayers: mechanics and flows. *Phys. Rev. E* **103**, 012405 (2021).
33. Schaller, V., Weber, C., Semmrich, C., Frey, E. & Bausch, A. R. Polar patterns of driven filaments. *Nature* **467**, 73–77 (2010).
34. Lushi, E., Wioland, H. & Goldstein, R. E. Fluid flows created by swimming bacteria drive self-organization in confined suspensions. *Proc. Natl Acad. Sci. USA* **111**, 9733–9738 (2014).
35. Doxzen, K. et al. Guidance of collective cell migration by substrate geometry. *Integr. Biol.* **5**, 1026 (2013).
36. Fürthauer, S., Neef, M., Grill, S. W., Kruse, K. & Jülicher, F. The Taylor–Couette motor: spontaneous flows of active polar fluids between two coaxial cylinders. *New J. Phys.* **14**, 023001 (2012).
37. Hobson, C. M. et al. Correlating nuclear morphology and external force with combined atomic force microscopy and light sheet imaging separates roles of chromatin and lamin A/C in nuclear mechanics. *Mol. Biol. Cell* **31**, 1788–1801 (2020).
38. Collinsworth, A. M., Zhang, S., Kraus, W. E. & Truskey, G. A. Apparent elastic modulus and hysteresis of skeletal muscle cells throughout differentiation. *Am. J. Physiol. Cell Physiol.* **283**, C1219–C1227 (2002).
39. Da Costa, A. D. S. et al. Fibroblasts close a void in free space by a purse-string mechanism. Preprint at *bioRxiv* <https://doi.org/10.1101/2020.08.15.250811> (2020).
40. Barbazan, J. et al. Cancer-associated fibroblasts actively compress cancer cells and modulate mechanotransduction. Preprint at *bioRxiv* <https://doi.org/10.1101/2021.04.05.438443> (2021).
41. Gilbert, S. F. & Barresi, M. J. F. *Developmental Biology* 11th edn (Sinauer, 2016).
42. Sharples, A. P., Al-Shanti, N., Lewis, M. P. & Stewart, C. E. Reduction of myoblast differentiation following multiple population doublings in mouse C2C12 cells: a model to investigate ageing? *J. Cell. Biochem.* **112**, 3773–3785 (2011).

**Publisher's note** Springer Nature remains neutral with regard to jurisdictional claims in published maps and institutional affiliations.

© The Author(s), under exclusive licence to Springer Nature Limited 2022

## Methods

**Cell culture and drug treatments.** C2C12 mouse myoblasts were cultured in DMEM media containing 4,500 mg l<sup>-1</sup> glucose, 1 mM sodium pyruvate (Life Technologies) and supplemented with 10% fetal bovine serum (FBS), 100 units per ml of penicillin and 100 µg ml<sup>-1</sup> streptomycin. Maximum passages were kept below 20. For starvation conditions, used to promote differentiation, we supplemented the same DMEM media with 2% horse serum. For inhibiting differentiation, C2C12 cells were used after 50–60 passages.

For inhibiting proliferation, cells were treated with Mitomycin-C (Sigma) at 10 µM at 1 h at 37 °C, then washed away and replaced by fresh medium. Imaging data were acquired up to 10 h after treatment with Mitomycin-C, to avoid toxic effects<sup>43</sup>.

For inhibiting contractility (myosin-II ATPase), cells were treated either with Blebbistatin (Sigma) at 17 µM or with the ROCK inhibitor Y-27632 (BioVision) at 25 µM.

In all treatments, DMSO concentration was kept below 10<sup>-3</sup>% v/v.

**Fluorescence labelling and imaging.** For fluorescence immunostaining of MyHC, cells were fixed with 4% paraformaldehyde (Sigma) in PBS for 10 min. Fixation time for 3D protrusions was set to 1 h. Cells were subsequently permeabilized for 30 min with 0.1% Saponin (Sigma) while blocked with 0.1% bovine serum albumin (BSA, Sigma). Finally, fixed cells were incubated with primary antibodies. Myosin-4 Monoclonal Antibody conjugated with Alexa Fluor 488 (MF20, Thermo Fisher) was incubated for 1 h at room temperature, at 5 µg ml<sup>-1</sup> (1:100 dilution) and 0.1% BSA.

Actin was labelled with SiR-actin (Spirochrome). Concentrations used were 1 µM (30 min incubation) for fixed samples and 100 nM (6 h incubation) for live imaging.

Cell nuclei were labelled after fixation with Hoechst 33342 (Thermo Fisher) at 10 µg ml<sup>-1</sup> (5 min incubation).

Fixed samples were imaged by using a Nikon Eclipse Ti-E microscope equipped with a Nikon A1 confocal unit. We used ×40/×60 water/oil immersion objectives (numerical aperture (NA) 1.15/1.4). The microscope was operated with NIS-Elements (v.4.60.00). A Zeiss LSM-710 upright confocal microscope (×40 objective, NA 0.75) was used for imaging the top and exterior of cellular protrusions. The microscope was operated with Zeiss Zen 2011.

**Optical clearing.** In-depth imaging of 3D tissue protrusions required optical clearing, which was performed by following a protocol designed to clear organoids<sup>44</sup>. In brief, protrusions were fixed with 4% paraformaldehyde (Sigma) for 30 min, and permeabilized with a solution of Tween-20 (Sigma) in PBS (0.1% v/v) for 10 min at 4 °C. Subsequently, we used a solution of BSA (0.2% w/v, Sigma) and Triton-100 (0.1% v/v, Sigma) in PBS, used for 15 min at 4 °C. Finally, protrusions were rinsed with PBS, and immersed in an optically-transparent solution composed of fructose (2.5 M, Sigma) and glycerol (60% v/v, Sigma) in PBS.

**Time-lapse imaging.** Time-lapse imaging was performed with an inverted microscope Nikon Ti-E installed into a thermostatically controlled chamber (Life Imaging Technologies) and equipped with a micro-incubator for thermal, CO<sub>2</sub> and humidity control (OKOLab). The microscope was also equipped with an automated stage and a Yokogawa CSU-W1 spinning disc unit. Image acquisition was performed with an Andor Zyla 4.2 Plus camera, operated with Slidebook (v.6.0.19). We performed fluorescence (×60 lens, NA 1.4), phase-contrast (×10/×20 objectives, NA 0.3/0.45) and differential interference contrast imaging (×20 lens, NA 0.45). Four-dimensional time-lapse was used for actin-labelled cell mounds (×60 lens, NA 1.4) and for the pillar compression experiments. The latter combined differential interference contrast and confocal fluorescence modes (×20 lens, NA 0.45). Typically, we acquired 12 images per hour for >10 h.

**Substrate functionalization and micropatterning.** To prepare surfaces for micropatterning, glass bottom dishes (Mattek) were first activated using a plasma cleaner (Harrick Plasma, PDC-32G) for 3 min. Then, the glass surface was treated with a 0.1 mg ml<sup>-1</sup> poly-lysine (PLL) (Sigma) solution for 30 min, then washed with HEPES buffer (pH 8.4). A solution of 50 mg ml<sup>-1</sup> methoxy polyethylene glycol (mPEG) (molecular weight 5,000), succinimidyl valerate (Laysan Bio) was applied to passivate the surface for 1.5 h, and then washed out with PBS. Substrates were normally used after preparation although they can be kept under PBS for 1–2 weeks at 4 °C.

Micropatterns were generated by using a ultraviolet (UV)-activated mPEG-scission reaction, spatially controlled by the system PRIMO (Alvéole)<sup>45</sup>, mounted on an inverted microscope Nikon Eclipse Ti-2. In the presence of a photo-initiator compound (PLPP, Alvéole), the antifouling properties of the PEGylated substrate are tuned by exposure to near-UV light (375 nm). After illumination (1,200 mJ mm<sup>-2</sup>) through a ×20 objective PLL is exposed. After rinsing with PBS, fibronectin (Calbiochem) was incubated at 50 µg ml<sup>-1</sup> at room temperature for 5 min to coat the PEG-free motifs with the cell-adhesive protein. The excess of fibronectin was washed out with PBS. PBS was finally replaced by medium, and a suspension of cells was added at densities of roughly 1 × 10<sup>5</sup> cells per cm<sup>2</sup>. Samples were kept in an incubator at 37 °C and 5% CO<sub>2</sub>. After 10–30 min, non-adhered cells were washed out.

**Micro-fabrication of hydrogel pillars.** To fabricate PEG-based fluorescent micropillars onto glass we used a photopolymerizable aqueous solution composed of fluorescent-PEG(2k)-acrylate, 4-arm-PEG(20k)-acrylate and the photo-initiator PLPP (Alvéole). For the preparation of the fluorescent-PEG(2k)-acrylate, Fluoresceinamine (Sigma) was dissolved at 0.1 mg ml<sup>-1</sup> in HEPES buffer solution (pH 8.3) and mixed with an equal volume of a 50 mg ml<sup>-1</sup> AC-PEG-(molecular weight 2,000)-succinimidyl valerate (Laysan Bio) solution, which was prepared in the same buffer. The resulting mixture was vortexed and let sit at room temperature in the dark for 1 h. The photopolymerizable solution was then prepared by dissolving 4-arm-PEG-(molecular weight 20,000)-AC (Laysan Bio) in a 14 mg ml<sup>-1</sup> PLPP solution at the desired concentration (2.5% w/v to obtain gels of stiffness 4 kPa) with 10% of the 25 mg ml<sup>-1</sup> solution of fluorescent PEG(2k)-acrylate. To prepare the pillars, the photopolymerizable solution was placed between plasma-treated glass and a 150-µm-thick polytetrafluoroethylene film separated by spacers composed of the same film. Subsequently, photopolymerization of pillars was performed by illuminating the top surface of the glass with full circle motifs of UV light (100–200 mJ mm<sup>-2</sup>) with the system PRIMO (Alvéole). After polymerization, the pillars were rinsed with deionized water. We then PEGylated the surface and micropatterned it with rings that enclosed the micropillars (Extended Data Fig. 7a).

**Image and data analysis.** Igor Pro (v.7.08) was used for representing the data in 2D plots. MATLAB R2017a (v.9.2) was used for generating velocity and orientation vector fields as well as for representing data in 3D plots.

**Nearest neighbour distance between half-integer defects.** For the detection of half-integer defects for the nearest-neighbour analysis in Fig. 1b we first define as defect areas, the regions where the parameter  $\sqrt{\langle \cos^2 \theta \rangle + \langle \sin^2 \theta \rangle}$  was below a threshold value. The brackets  $\langle \rangle$  denote an average over a local region. To assess their topological strength, we calculated the winding number  $\frac{\sum \Delta \theta}{2\pi}$ , where  $\sum \Delta \theta$  is the accumulated rotation of the orientational field around these low-order regions<sup>46</sup>. Finally, for the nearest neighbour distance analysis, we compared all the distances between defects and selected the minimum values corresponding to each pair.

**Flow, orientation and associated quantities.** Tracer-free velocimetry analysis of the flows in the cell monolayers was performed with a public domain PIV program implemented as an ImageJ plugin<sup>30</sup>. In particular, we used the (basic) iterative PIV with three passes, with decreasing interrogation window size. Minimum window sizes used in the analysis were normally set at 10 × 10 µm, which show good qualitative agreement with our experimental observations. Temporal resolution was set to a minimum of 5 or 10 min between frames.

The Manual Tracking plugin for ImageJ was used to manually track trajectories of cells in Figs. 1a and 2a,e.

The 2D orientational field in cell monolayers was extracted by using the plugin OrientationJ (v.2.0.5) for ImageJ, which is based on the structure tensor method<sup>39</sup>. In brief, for each pixel of an image, intensity gradients are computed. A structure matrix is obtained from the products of the components of the intensity gradients that are averaged in local subwindows. For most of the cases, subwindow size was set to 6 × 6 µm. Diagonalization of this structure matrix results in two eigenvectors per pixel. The eigenvector with the smallest eigenvalue represented the direction of smallest variation of the intensity map in the vicinity of the pixel and was associated with the main orientation. Finally, orientations were then typically averaged in image subwindows of 12 × 12 µm. The amplitude of the orientation vectors, named coherency C, was also extracted from OrientationJ. Note that the coherency associated to orientation vectors is informative of relative changes in space but cannot be compared between different images.

Further analyses were performed with custom-written MATLAB codes.

The spatial nematic autocorrelation function  $C_{nn}$  (Fig. 1b and Extended Data Fig. 1) was calculated from each orientational field position as

$$C_{nn}(d) = 2 \left( \langle \cos^2(\theta(r) - \theta(r+d)) \rangle - \frac{1}{2} \right) \quad (1)$$

where  $\theta$  is the local orientation of  $n$  with respect to a fixed axis. We considered  $C_{nn}$  at time points within a 1 h period for temporal averaging. The characteristic nematic length  $\xi_{nn}$  was extracted from the intersection of the initial linear decay and  $C_{nn} = 0$ .

The angle  $\psi$  was obtained for each position as the angle between the orientation vectors  $\mathbf{n}$  and their corresponding radial direction vectors  $\mathbf{r}$ . Unless stated otherwise, for the calculation of  $\psi$ , we considered only  $\mathbf{n}$  vectors at distances  $r < 0.9R$ , where  $R$  is the radius of the islands, and with associated  $S > 0.4$ . Only in Extended Data Fig. 6 did we consider just the vectors  $\mathbf{n}$  at distances  $0.65R < r < 0.85R$ . The threshold for  $S$  was kept at  $S > 0.4$ .

The angle  $\beta$  was obtained for each position from the scalar product between the orientation vectors  $\mathbf{n}$  and their corresponding velocity vectors  $\mathbf{v}$ .

To obtain the orientational order parameter  $S$ , we first computed the nematic order tensor  $Q$  from the orientational field  $\mathbf{n}$ . Specifically, the components of the nematic tensor were

$$Q_{xx} = 2C\cos(2\theta) \quad (2)$$

$$Q_{xy} = 2C\sin(2\theta) \quad (3)$$

where  $C$  corresponds to the coherency and  $\theta$  is the local orientation of  $\mathbf{n}$  with respect to a fixed axis. The orientational order parameter  $S$  was calculated from the time-averaged components of the nematic tensor  $Q$  for each position as

$$S(x, y) = \frac{\sqrt{\langle Q_{xx} \rangle_{x,y}^2 + \langle Q_{xy} \rangle_{x,y}^2}}{2} \quad (4)$$

where the brackets  $\langle \rangle$  denote a time average over a local position in the space matrix.

**3D director field from fluorescence confocal z-stacks.** 3D-orientation analysis was based on a generalization of the above-mentioned method to intensity maps in 3D and it was implemented as a MATLAB function. In the following, we explain the procedure to determine the 3D director field  $\mathbf{n}$  from z-stacks of fluorescence images.

Let us consider a 3D intensity map  $I(x,y,z)$ , such as a z-stack of fluorescence images, where  $(x,y,z)$  represent the Cartesian coordinates. First, using the MATLAB function interp3, we interpolated the 3D intensity map  $I(x,y,z)$  so that the resolution of the  $z$  coordinate matched the resolution of the  $(x,y)$ -planes. Next, we used the MATLAB function imgaussfilt3 to apply a Gaussian filter with standard deviation  $\sigma_1$  on  $I(x,y,z)$ . This part eliminated small-wavelength fluctuations from the intensity map. For each pixel, we computed the gradient of the intensity map  $(\partial_x I, \partial_y I, \partial_z I)$  by using the MATLAB function imgradientxyz. We computed the structure matrix, which is defined as

$$\mathcal{M} = \begin{pmatrix} \langle \partial_x I \times \partial_x I \rangle & \langle \partial_x I \times \partial_y I \rangle & \langle \partial_x I \times \partial_z I \rangle \\ \langle \partial_y I \times \partial_x I \rangle & \langle \partial_y I \times \partial_y I \rangle & \langle \partial_y I \times \partial_z I \rangle \\ \langle \partial_z I \times \partial_x I \rangle & \langle \partial_z I \times \partial_y I \rangle & \langle \partial_z I \times \partial_z I \rangle \end{pmatrix} \quad (5)$$

where the brackets  $\langle \rangle$  denote a second Gaussian filter with standard deviation  $\sigma_2$ . We defined the traceless structure matrix as  $\bar{\mathcal{M}} = \mathcal{M} - \text{Tr}(\mathcal{M})\mathbb{I}/3$ , where  $\text{Tr}$  denotes the trace operator and  $\mathbb{I}$  denotes the identity matrix. For each pixel, the matrix  $\bar{\mathcal{M}}$  was diagonalized by the MATLAB function eig. For each pixel, the three eigenvectors of  $\bar{\mathcal{M}}$  define, in general, an orthogonal basis. The eigenvector with the smallest eigenvalue represented the direction of smallest variation of the intensity map  $I(x,y,z)$  in the vicinity of the pixel  $(x,y,z)$ . We considered the director field  $\mathbf{n}$  parallel to the eigenvector with minimal eigenvalue. Note that, the orientation of  $\mathbf{n}$  was determined up to a sign, meaning that  $\mathbf{n} \rightarrow -\mathbf{n}$  were indistinguishable. We choose  $n_z$  to be positive. The amplitude of  $\mathbf{n}$  was set by the smallest eigenvalue of  $\bar{\mathcal{M}}$ . For each pixel, we computed the components of the nematic tensor field  $Q$  in cylindrical coordinates, taking as the centre the geometrical centre of the confining domains. Finally, we averaged the components of the nematic tensor field  $Q$  over time and experiments. In conclusion, the method presented two input parameters given by the standard deviations of two Gaussian filters, and outputted a nematic tensor field  $Q$  from a 3D intensity map  $I(x,y,z)$ .

To construct Fig. 3b, we apply the above-mentioned routine with the input parameters  $\sigma_1=1\text{ px}$  and  $\sigma_2=5\text{ px}$  to 3D time-lapse stacks of actin-stained cell mounds ( $N=8$ ) and obtained the averaged nematic tensor field  $Q$  in cylindrical coordinates. We binned the data in the radial direction so that 20 points are shown. To represent the data, we used the following procedure. First, for each data point, we computed the eigenvectors and eigenvalues of the binned nematic tensor field using eig. Next, for each data point, we constructed a 3D ellipsoid of revolution with the major axis proportional to the largest eigenvalue and the minor axes proportional to the mean of the two lowest eigenvalues. For each  $z$ -plane in Fig. 3b, only the 3D ellipsoids of revolution that had a trace of the binned nematic tensor larger than the mean of each plane, were shown.

**Characterization of cell number density in mounds.** Nuclei density in mounds was assessed by using MorphoGraphX (v.1.0)<sup>47</sup> on 3D confocal stacks of actin- and nuclei-labelled fixed mounds. The actin signal was used to extract two triangular meshes with points corresponding to the outer mounds' surface and to the mounds' base in contact with the substrate. These meshes were used to compute the top and bottom surfaces of mounds. Nuclei at a distance up to  $3\mu\text{m}$  from these surfaces were then manually counted to calculate the cell number density. The nuclei near the edges of the top and bottom surfaces were considered for both surfaces. These nuclei corresponded to  $12\pm4\%$  and  $13\pm4\%$  of the total number of nuclei for the bottom and top surfaces, respectively (mean  $\pm$  s.d.,  $N=15$ ).

MorphoGraphX was also used for the visualization of the rotating actin spiral on the mound's top surface shown in Supplementary Video 8. This was achieved by considering only the actin signal at a distance up to  $6\mu\text{m}$  from the top surface.

**Calculation of stresses from nuclei deformations.** Both the volume of nuclei and pillars were obtained by segmenting fluorescence confocal stacks with Imaris (Oxford Instruments, v.9.5.0). Further analyses were performed with custom written MATLAB codes.

For the calculation of stresses from nuclear deformations, we first calculated average nuclear volumes ( $V_r$ ) as a function of the radial distance  $r$  and computed the difference with respect to the average volume of the nuclei at the periphery ( $V_R$ ). We then considered the linear relation between pressure and the relative variation of nuclear volume<sup>48</sup>.

$$P(r) = -B \frac{V_r - V_R}{V_R} \quad (6)$$

For the nuclei, we considered an elastic bulk modulus ( $B$ ) of  $11\text{ kPa}$  (ref. <sup>38</sup>).

**Calculation of stresses from pillar deformations.** In the following, we derive the theoretical equation used to quantify the cellular forces exerted on deformable elastic pillars. The geometry of pillars is approximated by a cylinder of radius  $R$  and height  $h$ . Due to the symmetries of the cylinder, we focus on axisymmetric solutions (that is, independent on the azimuthal coordinate  $\theta$ ) and use cylindrical coordinates  $(r, \theta, z)$ . Furthermore, we consider that our deformable elastic pillars behave as a linear elastic material (Supplementary Fig. 9a), so that the stress tensor  $\sigma$  obeys

$$\sigma_{\alpha\beta} = \frac{E}{1+\nu} U_{\alpha\beta} + \frac{Ev}{(1+\nu)(1-2\nu)} U_{rr} \delta_{\alpha\beta} \quad (7)$$

where the symmetric part of the strain tensor is  $U_{\alpha\beta} = \frac{\partial_\alpha u_\beta + \partial_\beta u_\alpha}{2}$  with  $\mathbf{u}$  being the displacement vector. The material parameters are the elastic modulus  $E$  and the Poisson ratio  $\nu$ .

The force balance equation reads

$$\partial_\beta \sigma_{\alpha\beta} = 0 \quad (8)$$

as there are no bulk forces applied on the pillars.

To complete our description, we need to specify the boundary conditions. On the lateral surface of the cylinder, we consider that cells exert a uniform compressional stress  $-P$ , so that  $\sigma_{rr}(r=R) = -P$  and  $\sigma_{rz}(r=R) = 0$ . On the bottom surface of the cylinder, we consider vanishing displacement in the  $z$ -direction  $u_z(z=0) = 0$ . On the bottom surface, the cylinder is allowed to slide freely in the radial direction, so that  $\sigma_{rz}(z=h) = 0$ . On the upper surface of the cylinder, we consider stress-free conditions  $\sigma_{zz}(z=h) = 0$  and  $\sigma_{rz}(z=h) = 0$ .

A steady-state solution to the above problem, corresponds to a displacement field  $\mathbf{u}$  with  $u_r = U_r^0 r$ ,  $u_\theta = 0$  and  $u_z = U_z^0 z$ . In this case, the non-vanishing components of the stress tensor are:

$$\sigma_{rr} = \sigma_{\theta\theta} = \frac{E}{1+\nu} U_r^0 + \frac{Ev}{(1+\nu)(1-2\nu)} (2U_r^0 + U_z^0) \quad (9)$$

$$\sigma_{zz} = \frac{E}{1+\nu} U_z^0 + \frac{Ev}{(1+\nu)(1-2\nu)} (2U_r^0 + U_z^0) \quad (10)$$

By enforcing that  $\sigma_{zz}(z=h) = 0$  and  $\sigma_{rr}(r=R) = -P$ , we obtain the displacement field

$$u_r = -\frac{(1-\nu)P}{E} r \quad (11)$$

$$u_z = \frac{2\nu P}{E} z \quad (12)$$

Rewritten in terms of the areal strain,  $\frac{\Delta A}{A} = \frac{2u_r(r=R)}{R}$ , the stress reads

$$P = -\frac{E}{2(1-\nu)} \frac{\Delta A}{A_0} \quad (13)$$

where  $\Delta A$  is the difference of cylinder base' area after deformation and  $A_0$  is the area of the cylinder base before deformation. For the 2.5%w/v PEG pillars, we considered a Poisson ratio ( $\nu$ ) of 0.5 (ref. <sup>49</sup>) and an elastic modulus ( $E$ ) of  $4\text{ kPa}$  (Supplementary Note 5).

For the calculation of compressive stress as a function of time in Extended Data Fig. 7, the areal strain was calculated from the experimentally measured pillar volumes as

$$\left( \frac{\Delta A}{A_0} \right)_{\text{exp}} = \frac{V - V_0}{A_0 h_c} \quad (14)$$

where  $V$  corresponds to the volume of the cylindrical pillar up to a fixed height, typically  $40\mu\text{m}$ , which was larger than the height  $h_c$  up to which the cylindrical pillar was compressed. Temporal evolution of  $h_c$  was assessed manually from

3D volume renderings of the pillars.  $V_0$  and  $A_0$  correspond to the initial volume and base area of the cylindrical pillar, respectively. Because the areal strain was computed with respect to the stress-free state with volume  $V_0$ , this calculation led to absolute values of compressive stress.

For the calculation of compressive stress as a function of time in Fig. 5e, corresponding to myosin inhibition experiments, the areal strain was calculated from the experimentally measured pillar volumes as

$$\left( \frac{\Delta A}{A_0} \right)_{\text{exp}} = \frac{V - V_f}{V_f} \quad (15)$$

where  $V$  corresponds to the volume of the cylindrical pillar up to a fixed height and  $V_f$  corresponds to the final volume, 40 min after inhibition of myosin activity. Because the areal strain was computed with respect to a state with residual stresses and volume  $V_0$ , this calculation led to relative variations of compressive stress.

**Statistics and reproducibility.** All the reported results were obtained from experiments repeated successfully and independently 2–3 times in different weeks. Quantification always considered measurements from several cellular discs ( $N$ , indicated in the figure captions). Average vector fields (velocity and orientation) as well as the corresponding radial profiles were obtained by averaging >5 cellular discs per condition. Each cellular disc was imaged for at least 10 h every 5 min. For fixed cellular discs we considered >10 discs to be sufficient for the statistical analyses. No temporal averaging was applied to the data before the calculation of errors.

**Reporting Summary.** Further information on research design is available in the Nature Research Reporting Summary linked to this article.

## Data availability

The data that support the findings of this study are available in the Zenodo repository <https://doi.org/10.5281/zenodo.5549501>. High-resolution images and videos are available from the corresponding authors upon request.

## Code availability

The MATLAB code used for the 3D-orientation analysis is available in the Zenodo repository <https://doi.org/10.5281/zenodo.5680045>.

## References

43. Poujade, M. et al. Collective migration of an epithelial monolayer in response to a model wound. *Proc. Natl Acad. Sci. USA* **104**, 15988–15993 (2007).
44. Dekkers, J. F. et al. High-resolution 3D imaging of fixed and cleared organoids. *Nat. Protoc.* **14**, 1756–1771 (2019).
45. Strale, P. O. et al. Multiprotein printing by light-induced molecular adsorption. *Adv. Mater.* **28**, 2024–2029 (2016).
46. Huterer, D. & Vachaspati, T. Distribution of singularities in the cosmic microwave background polarization. *Phys. Rev. D* **72**, 043004 (2005).
47. Barbier de Reuille, P. et al. MorphoGraphX: a platform for quantifying morphogenesis in 4D. *eLife* **4**, e05864 (2015).
48. Guo, M. et al. Cell volume change through water efflux impacts cell stiffness and stem cell fate. *Proc. Natl Acad. Sci. USA* **114**, E8618–E8627 (2017).
49. Kloxin, A. M., Kloxin, C. J., Bowman, C. N. & Anseth, K. S. Mechanical properties of cellularly responsive hydrogels and their experimental determination. *Adv. Mater.* **22**, 3484–3494 (2010).

## Acknowledgements

We thank C. Roffay for suggesting the representation of 3D orientational fields and all the members from the Roux and Kruse groups for fruitful discussions and support. We thank S. Gabriele for useful insights on the elastic properties of C2C12 cell nuclei. P.G. acknowledges support from the Human Frontiers of Science Program (grant number LT-000793/2018-C). A.R. acknowledges funding from SystemsX RTD program EpiPhysX, the Swiss National Fund for Research grant numbers 31003A\_130520, 31003A\_149975 and 31003A\_173087, and the European Research Council Consolidator grant number 311536.

## Author contributions

P.G. and A.R. designed the research. P.G. performed the experiments. P.G. and C.B.-M. analysed the data. G.P. analysed cell number density in mounds. C.B.-M. and K.K. developed the theoretical model. All the authors participated in writing the manuscript.

## Competing interests

The authors declare no competing interests.

## Additional information

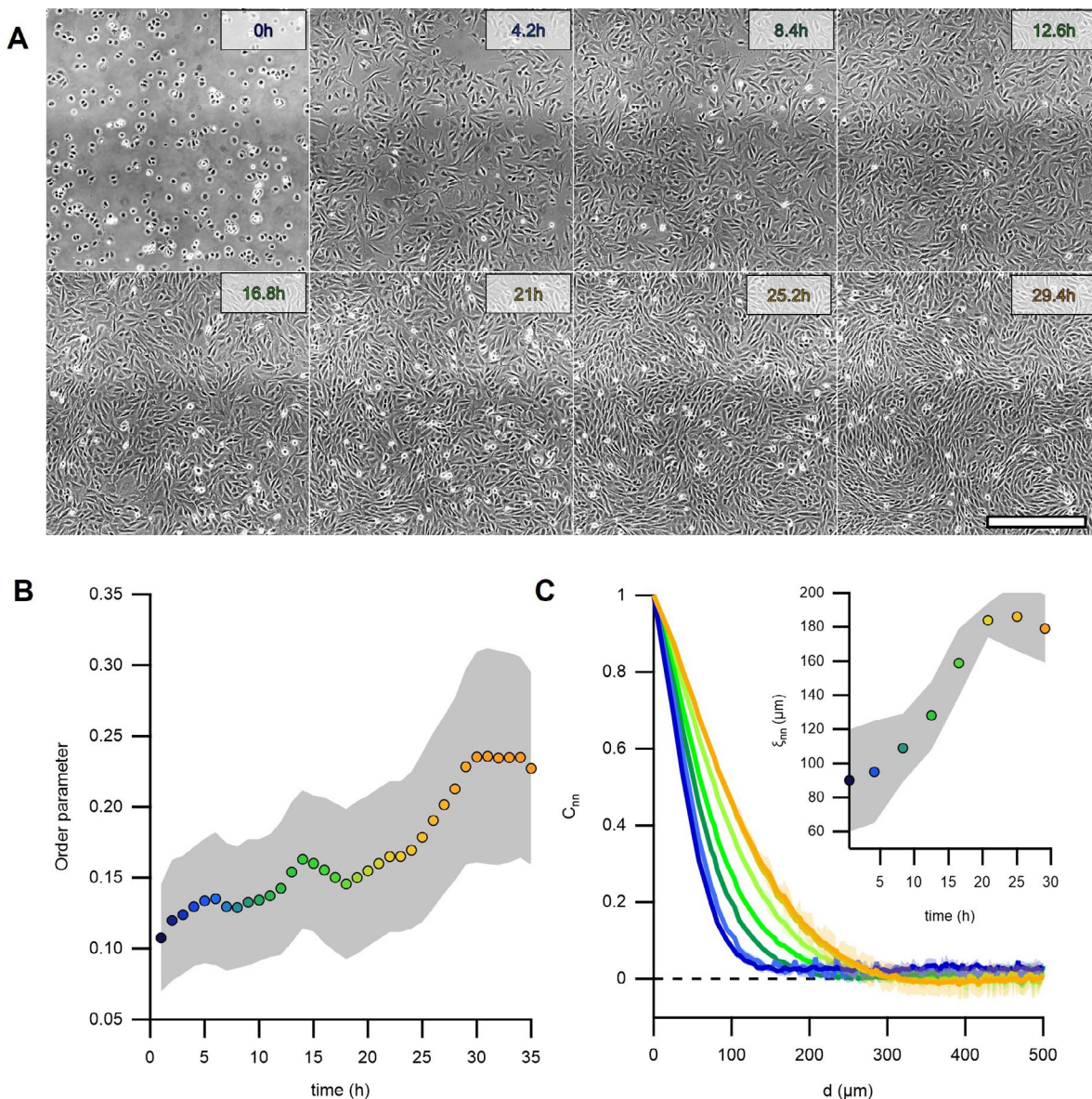
**Extended data** are available for this paper at <https://doi.org/10.1038/s41563-022-01194-5>.

**Supplementary information** The online version contains supplementary material available at <https://doi.org/10.1038/s41563-022-01194-5>.

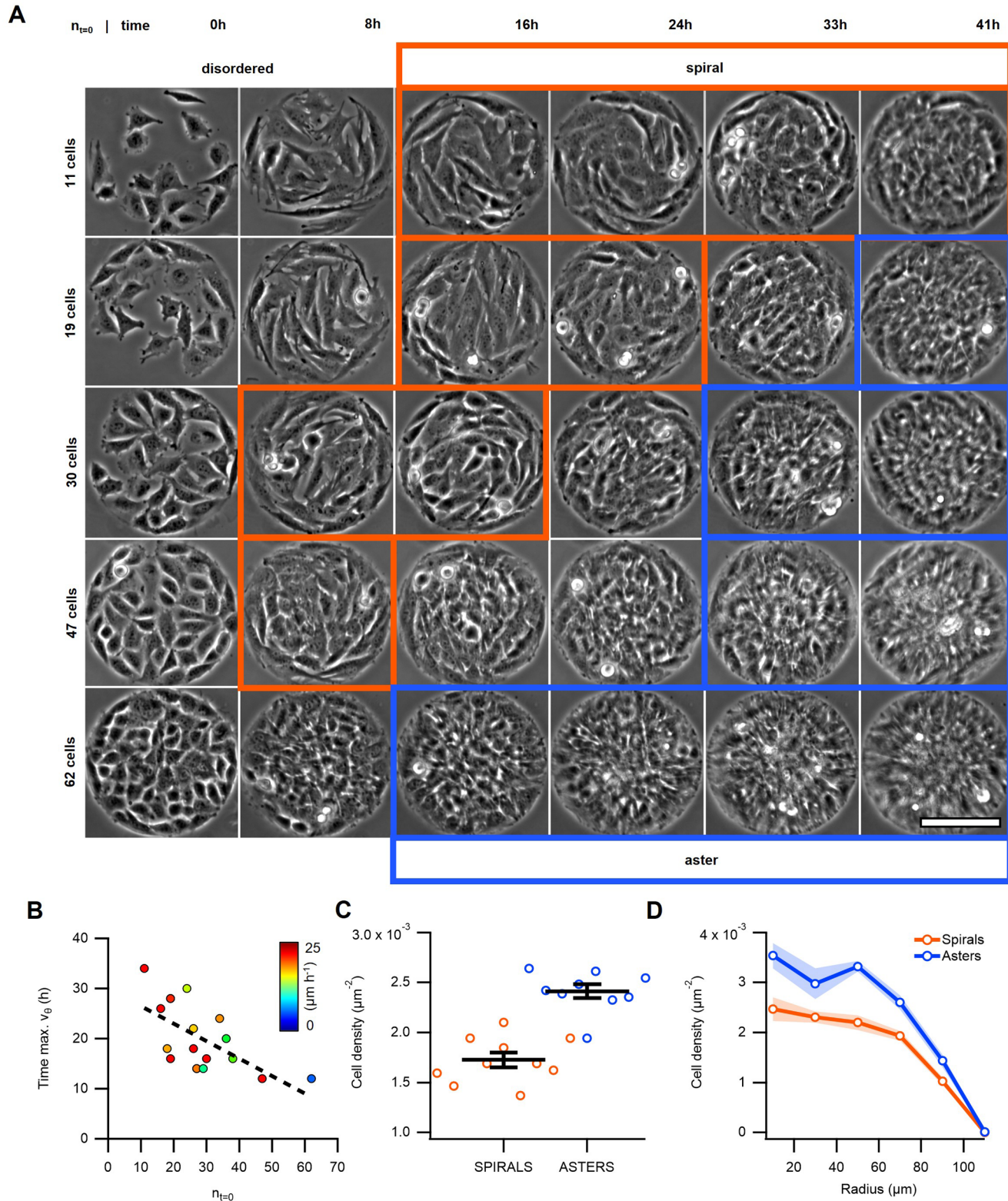
**Correspondence and requests for materials** should be addressed to Karsten Kruse or Aurélien Roux.

**Peer review information** *Nature Materials* thanks Marino Arroyo, Michael Murrell and the other, anonymous, reviewer(s) for their contribution to the peer review of this work.

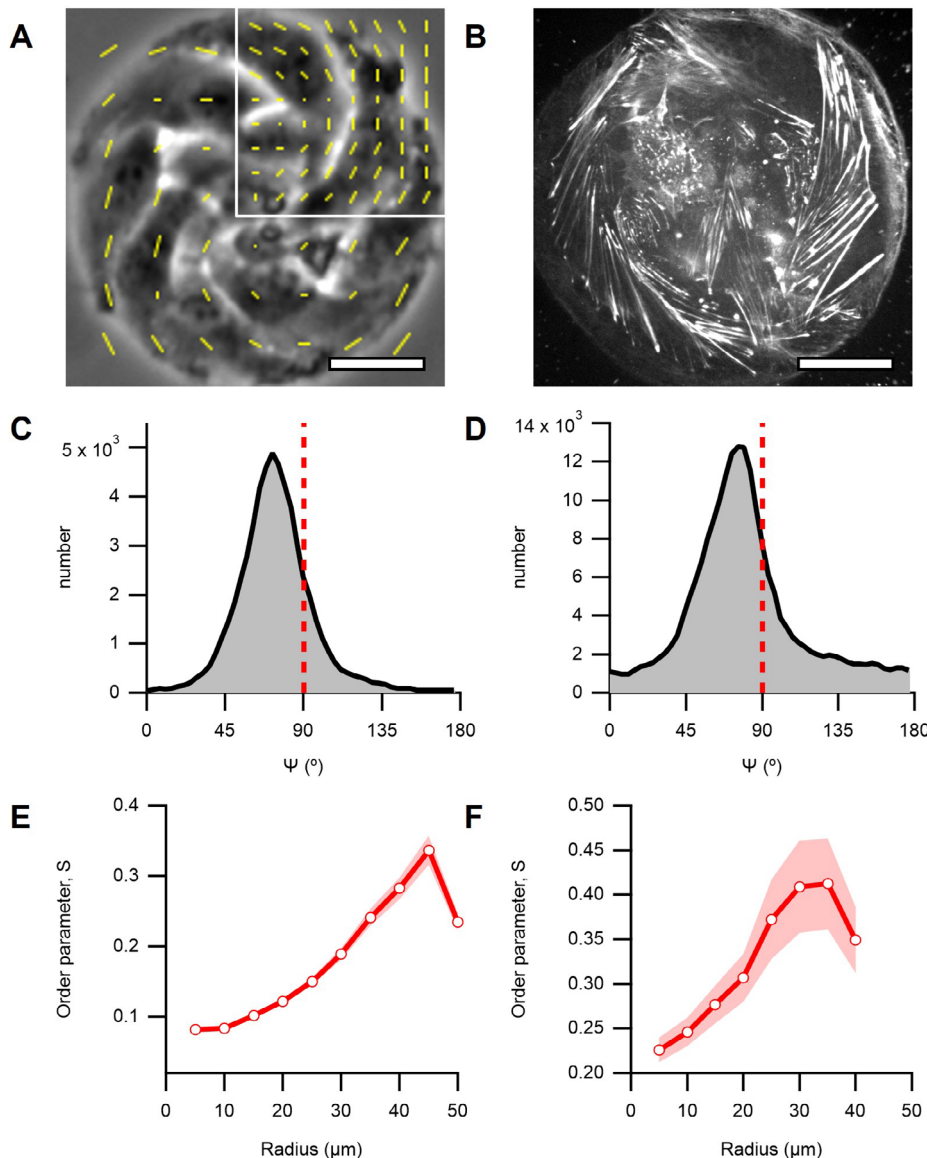
**Reprints and permissions information** is available at [www.nature.com/reprints](http://www.nature.com/reprints).



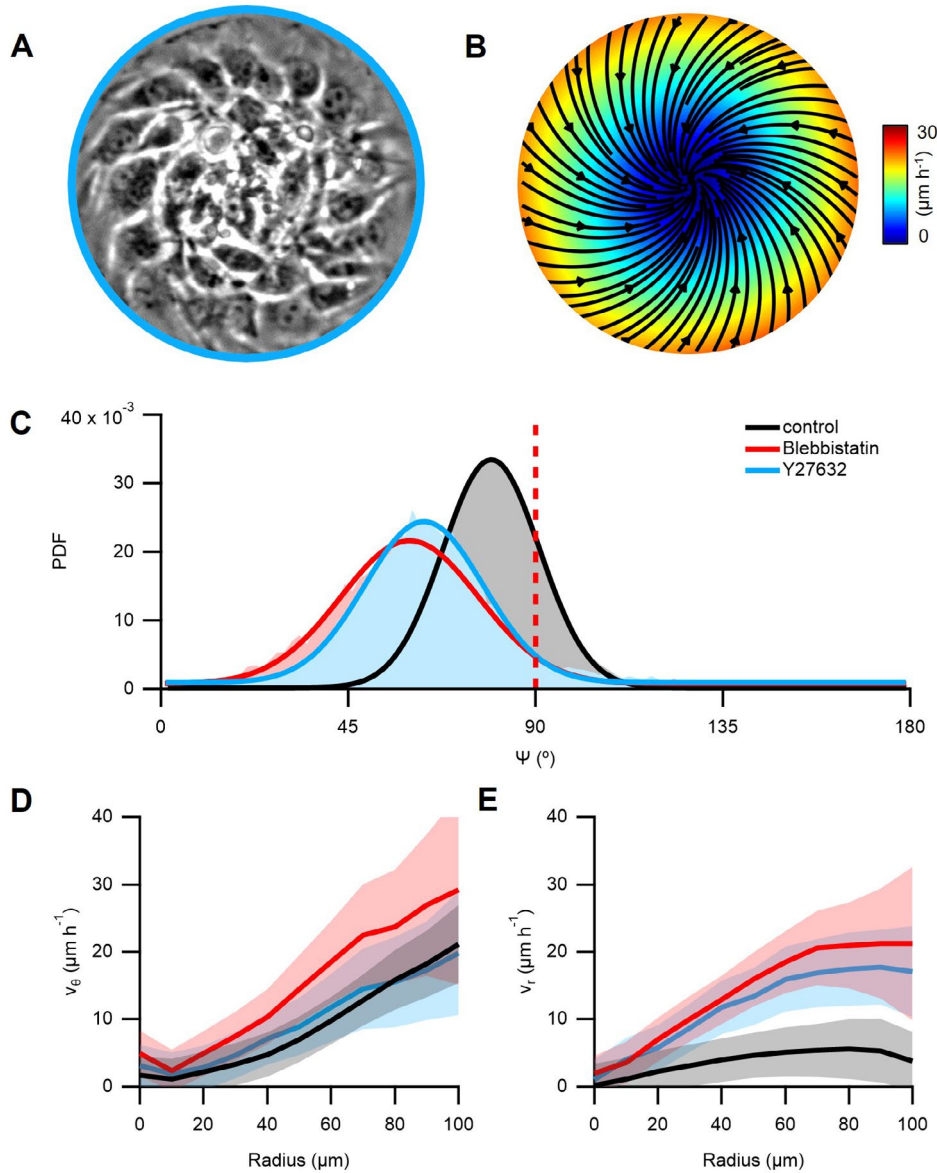
**Extended Data Fig. 1 | Formation of a nematic cellular monolayer.** **a**, Time series of a proliferating monolayer of C2C12 myocytes. Scale bar, 500  $\mu\text{m}$ . **b**, Average orientational order parameter as function of time. **c**, Two-point spatial autocorrelation function  $C_{nn}$  and nematic autocorrelation length  $\xi_{nn}$  (inset). Colors correspond to the time points indicated in the inset. Data are presented as mean values  $\pm$  s.d.



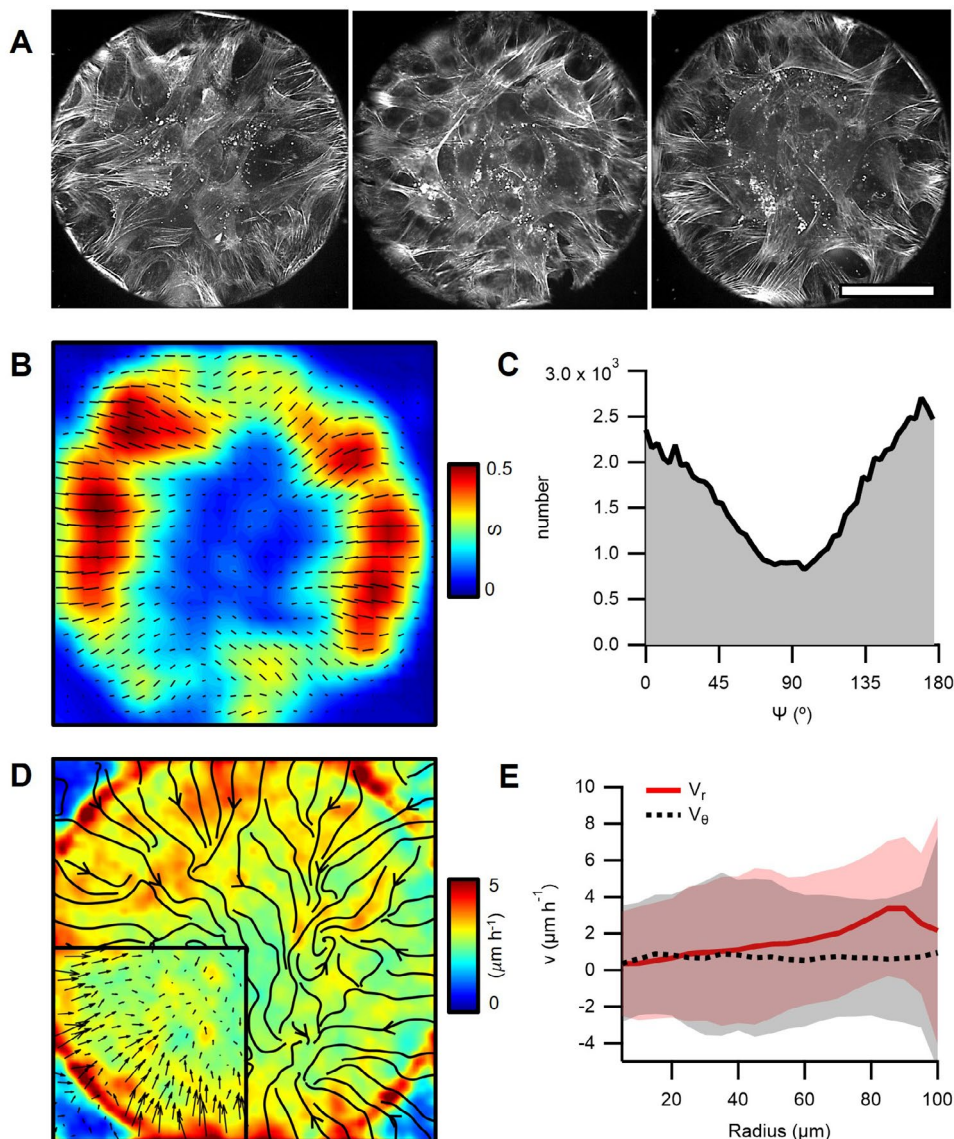
**Extended Data Fig. 2 | Cell number density for spirals and asters.** **a**, Time evolution of confined cell monolayers with different initial cell number. Scale bar, 100  $\mu\text{m}$ . **b**, Time of maximum tangential speed with respect of initial cell number. Colormap indicates speed. Dashed line corresponds to a linear fit. **c**, Average cell number density and **d**, radial density profiles for spirals ( $N = 10$ ) and asters ( $N = 9$ ). Data are presented as mean values  $\pm$  s.e.m.



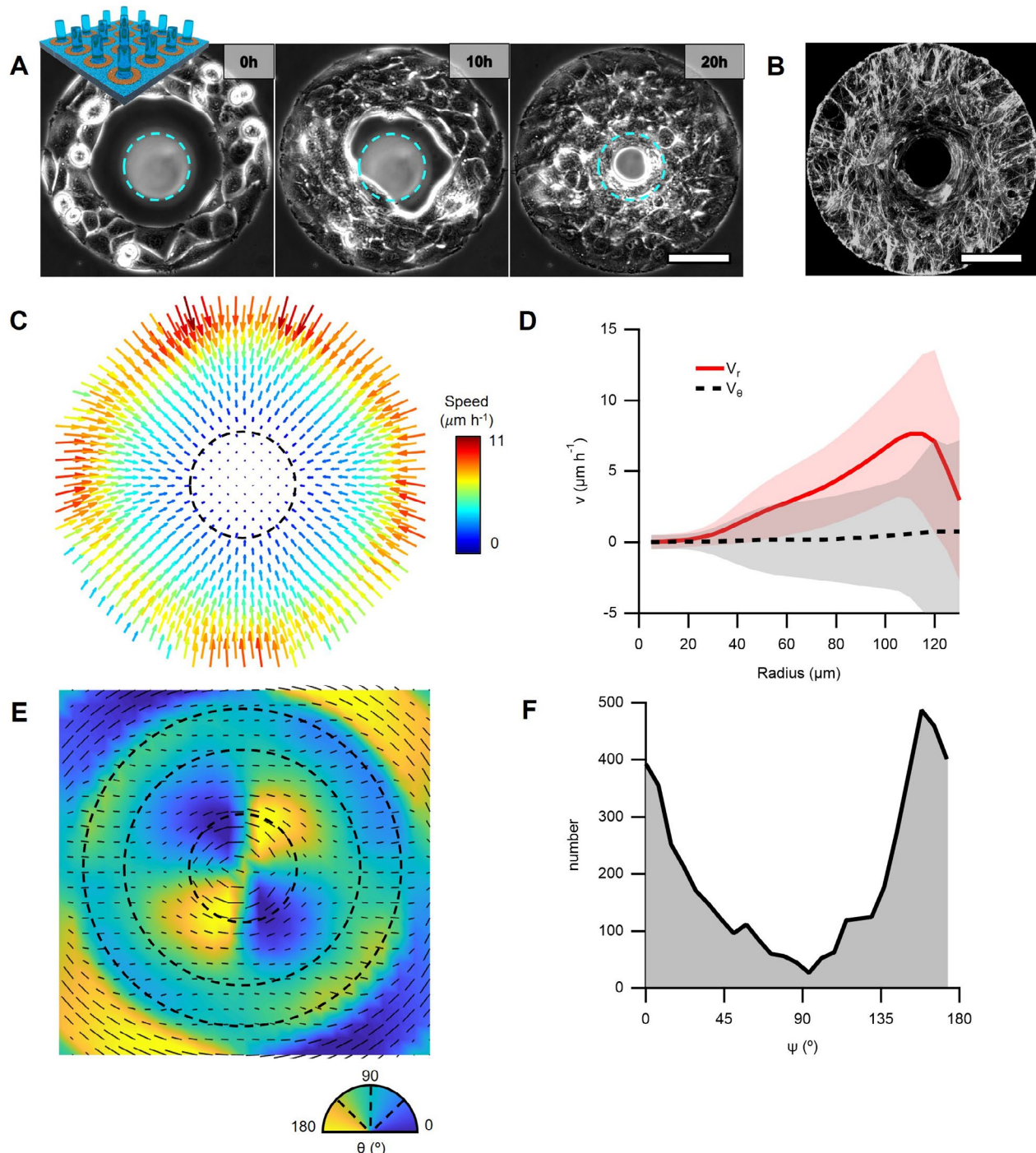
**Extended Data Fig. 3 | Orientational field from cell-shape and actin fibers in spirals.** **a**, Phase contrast image of a spiral. Yellow lines correspond to the local orientation. Vector length corresponds to the coherency (see Methods). For clarity, the totality of vectors is only shown in the inset. **b**, Confocal micrograph of the bottom plane of an F-actin-labelled spiral. Actin was stained with SiR-actin. Scale bars, 25 $\mu$ m. **c** and **d**, Distributions of the angle  $\psi$  extracted from phase contrast images ( $N=11$ ) and confocal micrographs ( $N=7$ ), respectively. The angle  $\psi$  is between the local director and the radial direction with respect to the geometrical center. In panels **c** and **d**, the red dashed line indicates  $\psi = 90^\circ$ . **e** and **f**, Radial profiles of the orientational order parameter  $S$  extracted from phase contrast images ( $N=11$ ) and confocal micrographs ( $N=7$ ), respectively. Data are presented as mean values  $\pm$  s.e.m.



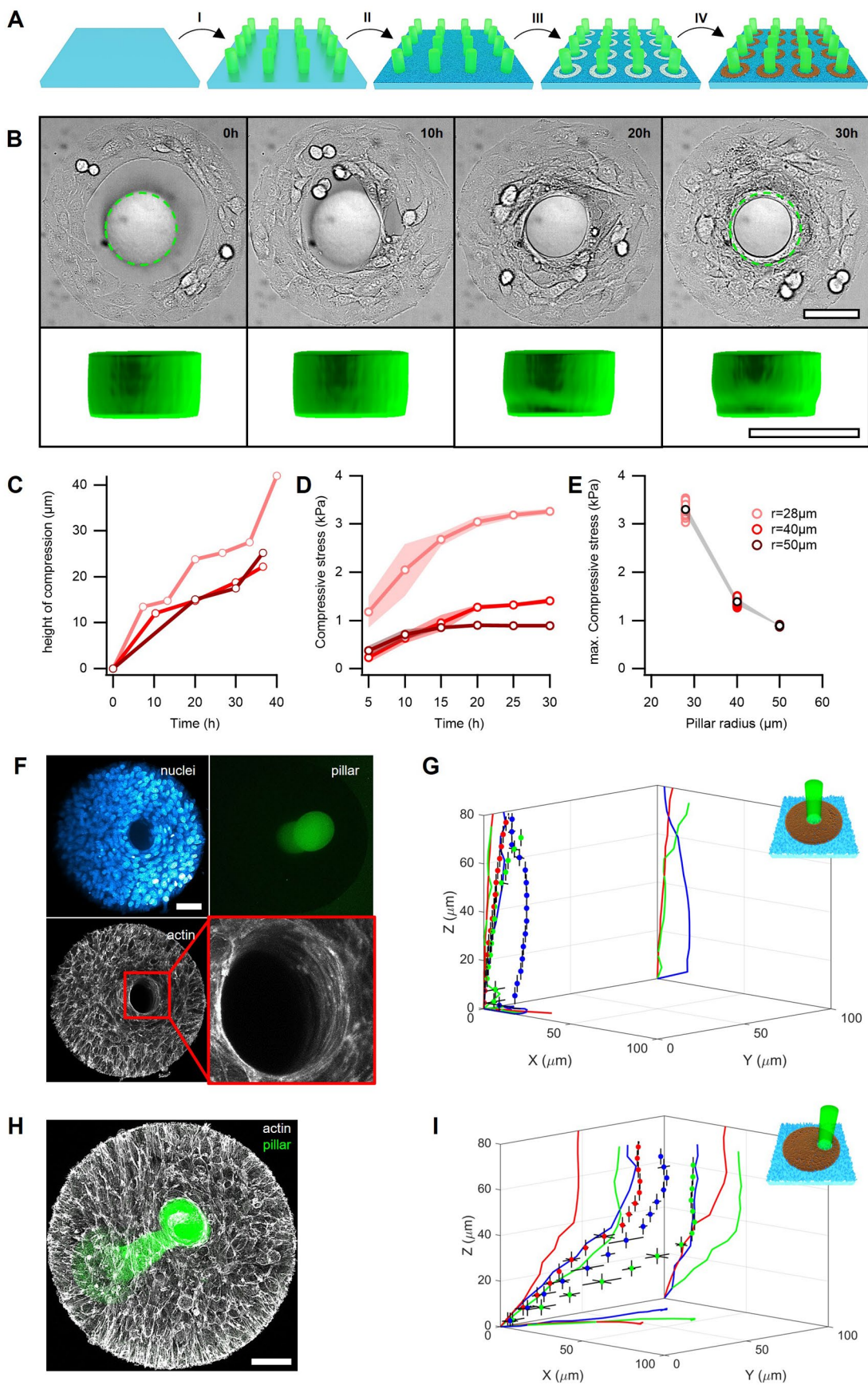
**Extended Data Fig. 4 | Influence of myosin activity on spiral morphology and dynamics.** **a**, Phase contrast image of a Y-27632-treated spiral. The confinement radius is 100  $\mu\text{m}$ . **b**, Average flow field for Y-27632-treated spirals. Streamlines are shown as black curves. The color code indicates the speed. **c**, Distributions of the angle  $\psi$  for spirals under different conditions.  $\psi$  is the angle between the local director and the radial direction with respect to the geometrical center. Dashed red line indicates  $\psi = 90^{\circ}$ . **d**, Radial profiles of the azimuthal and **e**, radial velocity components for spirals under the conditions corresponding to panel C. N = 11, 20 and 21, for control spirals, Y-27632-treated spirals, and Blebbistatin-treated spirals, respectively. Data are presented as mean values  $\pm$  s.e.m.



**Extended Data Fig. 5 | Actin flows in asters.** **a**, Confocal micrographs of actin at different aster bases. **b**, Average orientational field from time-lapses of asters in A ( $N=3$ ). Actin was stained with SiR-actin. Vector length corresponds to the coherency, showed as well as a colormap (see Methods). Scale bar,  $50\mu\text{m}$ . **c**, Distribution of the angle  $\psi$  extracted from confocal micrographs ( $N=3$ ). The angle  $\psi$  is between the local director and the radial direction with respect to the geometrical center. Dashed red line indicates  $\psi = 90^\circ$  ( $N=3$ ). **d**, Average flow field. Streamlines and vectors (inset) indicate the direction of actin flows. The colormap indicates the speed. **e**, Radial profiles of the radial (red) and azimuthal (black) velocity components. Data are presented as mean values  $\pm$  s.e.m.

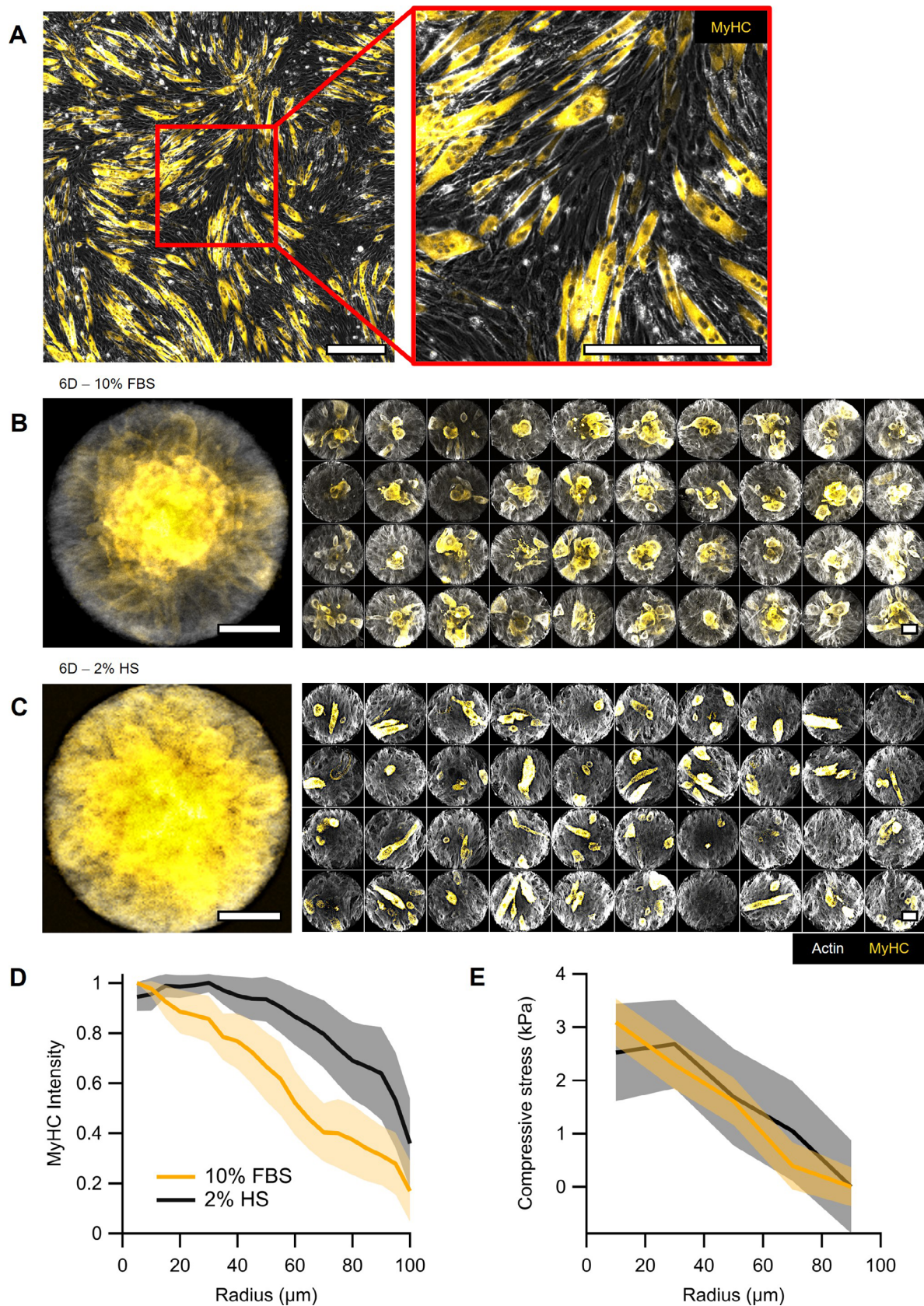


**Extended Data Fig. 6 | Aster arrangements and rings at the pillars' base.** **a**, Time-series of a C2C12 cell monolayer initially positioned on a circular ring constricting a hydrogel micro-pillar. Cyan dashed line indicates the initial pillar section. A schematic of the setting is included as an inset. **b**, Actin-stained cells after constriction show an aster arrangement. Actin was stained with SiR-actin. **c**, Average flow field around pillars during constriction ( $N=9$ ). The color scale corresponds to the speed. **d**, Radial profiles of the radial (red) and azimuthal (black) velocity components. Data are presented as mean values  $\pm$  s.e.m. **e**, Average orientational field. For clarity, only half of the total number of orientation vectors are shown. The color scale represents the angle of the director with respect to the horizontal axis. Dashed circles mark the position of the pillar section and the initial ring. Vector length corresponds to the coherency (see Methods). **f**, Distribution of the angle  $\psi$  between the local director and the radial direction with respect to the geometrical center. Scale bars, 50  $\mu\text{m}$ .



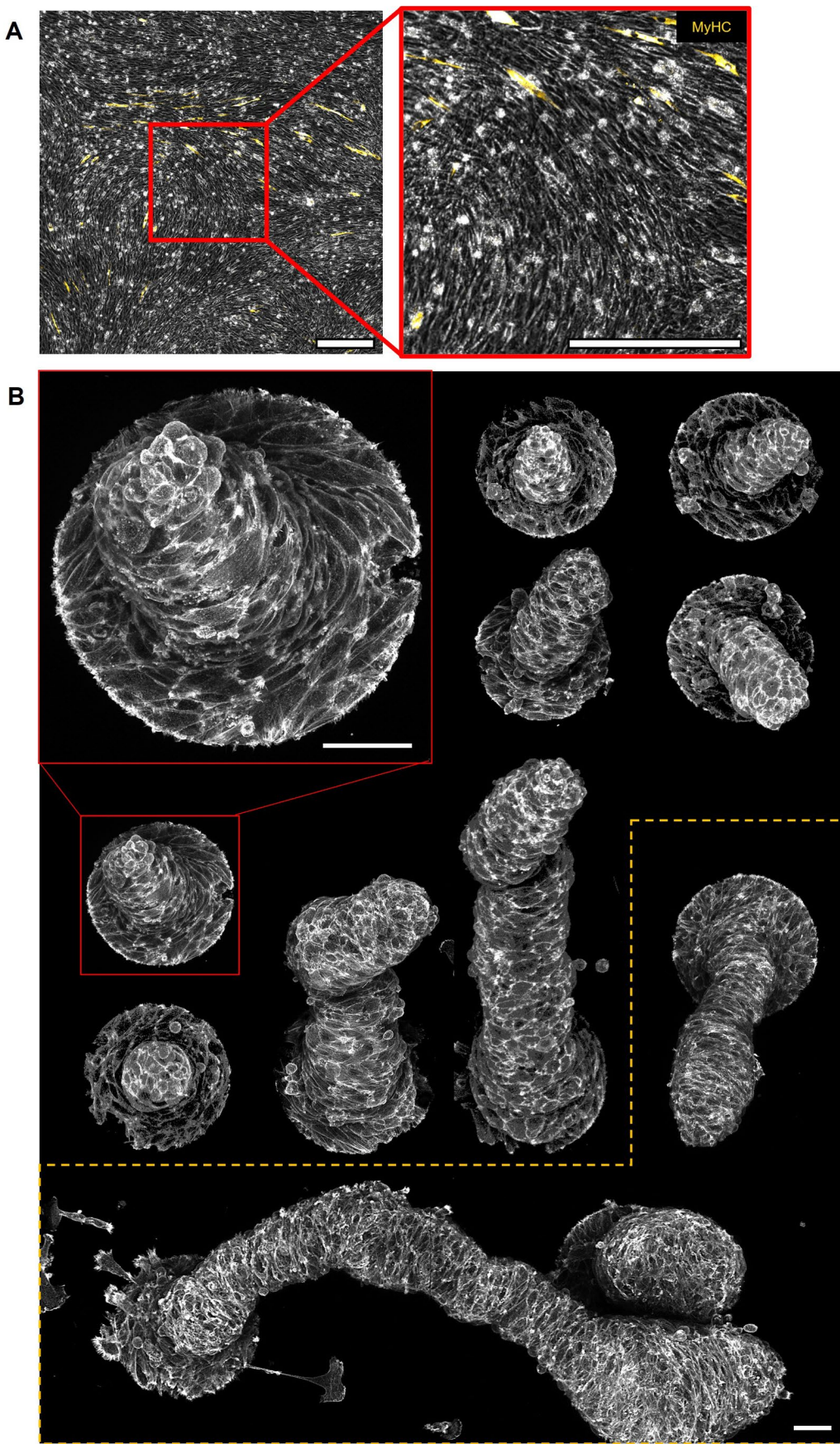
Extended Data Fig. 7 | See next page for caption.

**Extended Data Fig. 7 | Compression dynamics of hydrogel pillars.** **a**, Schematics of the protocol employed to fabricate cell-adhesive rings enclosing passive fluorescent hydrogel micro-pillars. After activation of the glass substrate, micro-pillars were fabricated by illuminating a photo-polymerizable mPEG solution with disk patterns of UV light with an inverted microscope (step I). Then, the substrate was functionalized with PLL-PEG (step II). PEG chains were locally photo-degraded by illuminating the substrate with ring patterns of UV light (step III). Finally, fibronectin was incubated (step IV). **b**, Time-series showing the compression of a pillar. Green dashed line on bright-field images depicts the initial size of the pillar section close to the base with a radius of  $r=40\mu\text{m}$ . The radius of the cellular island is  $100\mu\text{m}$ . 3D rendering of the pillar is shown below. **c**, Temporal evolution of the height up to which pillars are compressed for different radii. **d**, Compressive stress for pillars with different radii. Data are presented as mean values  $\pm$  s.e.m. **e**, Maximum compressive stress vs pillar radii. For panels C, D and E, the radius of pillars ( $r$ ) is indicated in the legend of panel E. **f**, Maximum Z projections of a confocal stack of a mound deforming a centred pillar. **g**, Position of the centroid of the sections of 2 centered pillars (Green and blue). Green curves correspond to the pillar in F. Red curves correspond to a pillar without cells around it. **h**, Maximum Z projection of a confocal stack of a mound deforming a non-centered pillar. **i**, Position of the centroid of the sections of 3 non-centered pillars. Green curves correspond to the pillar in H. For G and I, centroids of the pillar base are positioned at the origin. Data are presented as mean values  $\pm$  s.d. Actin was stained with SiR-actin. Nuclei were stained with Hoechst 33342. Scale bars,  $50\mu\text{m}$ .



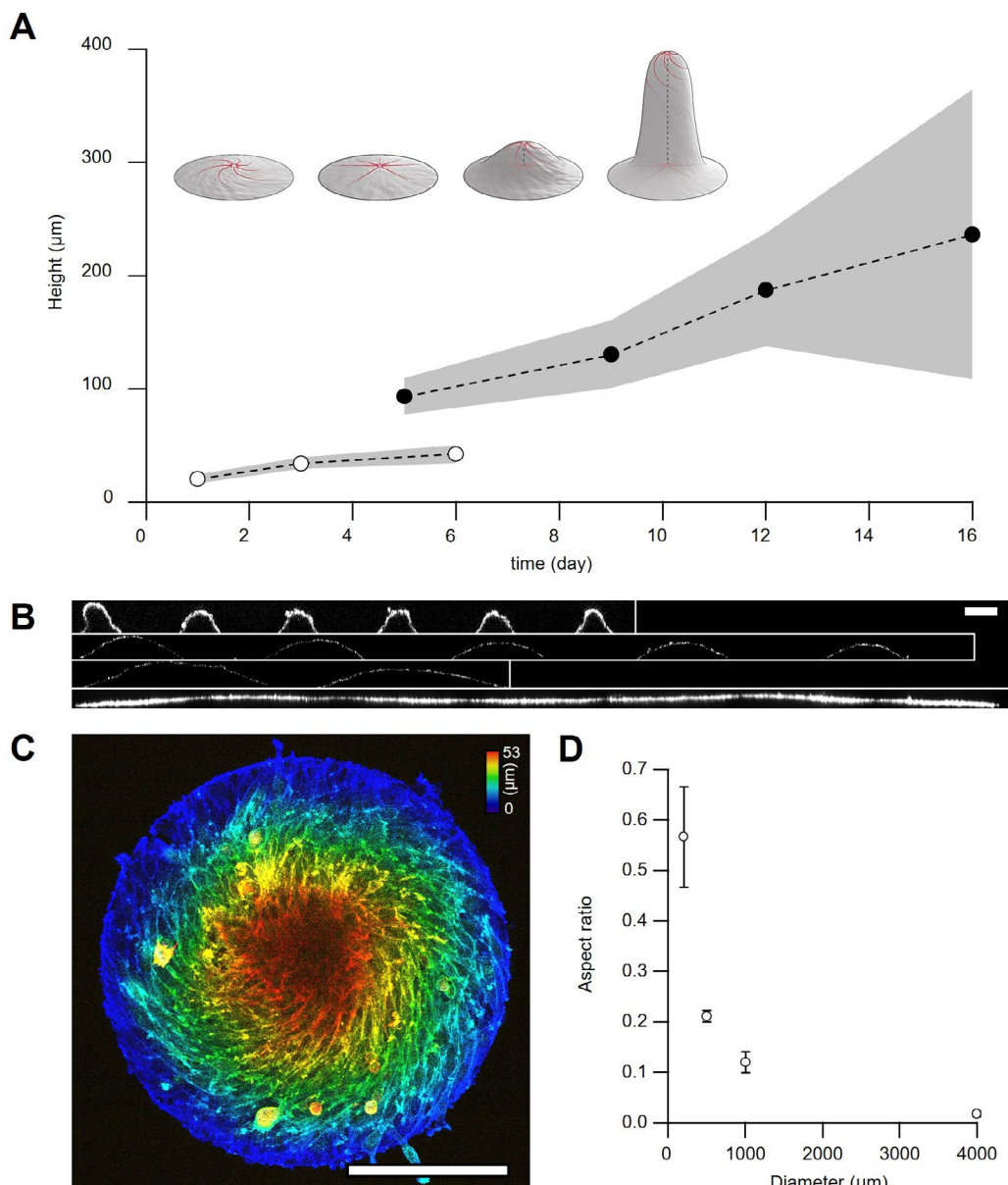
Extended Data Fig. 8 | See next page for caption.

**Extended Data Fig. 8 | Localization of myosin heavy chain expression.** **a**, Image composites of phase contrast and fluorescence images of confluent monolayers of C2C12 cells competent for differentiation, after 6 days under starvation conditions (see Methods). Right panel corresponds to a zoomed region from the left panel. Scale bars, 500 $\mu$ m. **b**, Average projection of confocal micrographs of cellular islands ( $N=40$ , base radius of 100 $\mu$ m) grown for 6 days in complete medium (10% FBS). Individual micrographs are shown in the panels on the right. **c**, Average projection of confocal micrographs of cellular islands ( $N=40$ , base radius of 100  $\mu$ m) grown for 6 days under starvation conditions (2% HS). Individual micrographs are shown in the panels on the right. For all panels, actin is shown in white, and myosin heavy chain (MyHC) is shown in yellow. Actin was stained with SiR-actin. MyHC was stained with the Myosin-4 Monoclonal Antibody conjugated with Alexa Fluor 488. Scale bars, 50 $\mu$ m. **d**, Radial profiles of averaged MyHC intensity and **e**, compressive stress under normal (orange) and starvation (black) conditions. Compressive stresses were measured from nuclear volume deformations. Data are presented as mean values  $\pm$  s.e.m.



Extended Data Fig. 9 | See next page for caption.

**Extended Data Fig. 9 | Cellular protrusions.** **a**, Image composites of phase contrast and fluorescence images of confluent monolayers of C2C12 cells incompetent for differentiation, after 6 days under starvation conditions (see Methods). Right panel corresponds to a zoomed region from the left panel. Scale bars, 500 $\mu$ m. MyHC was stained with the Myosin-4 Monoclonal Antibody conjugated with Alexa Fluor 488. **b**, Z-projections of actin of 14- (above yellow dashed line) and 16- (below yellow dashed line) days-old cellular protrusions. Red frame corresponds to a zoomed protrusion. Actin was stained with SiR-actin. Scale bars, 50 $\mu$ m.



**Extended Data Fig. 10 | Growth of cellular mounds and protrusions.** **a**, Average height of C2C12 islands of radius  $100 \mu\text{m}$  for different time points after the onset of confluence. White symbols (○) correspond to islands of differentiation-competent cells ( $N=17, 10, 16$ , for mounds at 1, 3, 6 days after the onset of confluence, respectively). Black symbols (●) correspond to islands of differentiation-incompetent cells ( $N=42, 11, 10$  and  $27$ , for mounds at 5, 9, 12, and 16 days after the onset of confluence, respectively). Data are presented as mean values  $\pm$  s.d. Inset: scheme of the time evolution of cellular nematic architectures from 2D to 3D. **b**, XZ section of mounds under different confinement sizes. The number of mounds in the images is 6, 5, 2 and 1 for diameters of  $200, 500, 1000$  and  $4000 \mu\text{m}$ , respectively. Mounds were labelled with Sir Actin. **c**, Z projection of an actin labelled 6 day old mound with a diameter of  $500 \mu\text{m}$ . Colormap indicates height. **d**, Aspect ratio of the mounds, calculated as height/diameter, for the different confinement sizes ( $N=30, 16, 4$  and  $5$  for diameters of  $200, 500, 1000$  and  $4000 \mu\text{m}$ , respectively). Data are presented as mean values  $\pm$  s.d. Scale bars,  $200 \mu\text{m}$ .

## Reporting Summary

Nature Portfolio wishes to improve the reproducibility of the work that we publish. This form provides structure for consistency and transparency in reporting. For further information on Nature Portfolio policies, see our [Editorial Policies](#) and the [Editorial Policy Checklist](#).

### Statistics

For all statistical analyses, confirm that the following items are present in the figure legend, table legend, main text, or Methods section.

n/a Confirmed

- The exact sample size ( $n$ ) for each experimental group/condition, given as a discrete number and unit of measurement
- A statement on whether measurements were taken from distinct samples or whether the same sample was measured repeatedly
- The statistical test(s) used AND whether they are one- or two-sided  
*Only common tests should be described solely by name; describe more complex techniques in the Methods section.*
- A description of all covariates tested
- A description of any assumptions or corrections, such as tests of normality and adjustment for multiple comparisons
- A full description of the statistical parameters including central tendency (e.g. means) or other basic estimates (e.g. regression coefficient) AND variation (e.g. standard deviation) or associated estimates of uncertainty (e.g. confidence intervals)
- For null hypothesis testing, the test statistic (e.g.  $F$ ,  $t$ ,  $r$ ) with confidence intervals, effect sizes, degrees of freedom and  $P$  value noted  
*Give P values as exact values whenever suitable.*
- For Bayesian analysis, information on the choice of priors and Markov chain Monte Carlo settings
- For hierarchical and complex designs, identification of the appropriate level for tests and full reporting of outcomes
- Estimates of effect sizes (e.g. Cohen's  $d$ , Pearson's  $r$ ), indicating how they were calculated

*Our web collection on [statistics for biologists](#) contains articles on many of the points above.*

### Software and code

Policy information about [availability of computer code](#)

Data collection Imaging: NIS-Elements-AR (ver. 4.60.00), SlideBook (ver. 6.0.19), Zeiss Zen 2011

Data analysis - Image pre-processing, particle image velocimetry (PIV), 2D orientational field analysis (ImageJ ver. 1.52p, OrientationJ plugin ver. 2.0.5), and 3D orientational field analysis (Matlab R2017a).  
- Custom analysis codes for the analysis of PIV and 2D Orientation data: Matlab R2017a (ver. 9.2)  
- Plots and statistics: Igor Pro (ver. 7.08)  
- Volume segmentation: Imaris (ver. 9.5.0)  
- Cell density in 3D and projection of curved surfaces from fluorescence stacks: MorphoGraphX (ver. 1.0)

For manuscripts utilizing custom algorithms or software that are central to the research but not yet described in published literature, software must be made available to editors and reviewers. We strongly encourage code deposition in a community repository (e.g. GitHub). See the Nature Portfolio [guidelines for submitting code & software](#) for further information.

### Data

Policy information about [availability of data](#)

All manuscripts must include a [data availability statement](#). This statement should provide the following information, where applicable:

- Accession codes, unique identifiers, or web links for publicly available datasets
- A description of any restrictions on data availability
- For clinical datasets or third party data, please ensure that the statement adheres to our [policy](#)

The data that support the findings of this study can be found in the Zenodo repository 10.5281/zenodo.5549501.

The codes used for the data analyses are available from the corresponding authors (A.R. and K.K.) upon reasonable request.

# Field-specific reporting

Please select the one below that is the best fit for your research. If you are not sure, read the appropriate sections before making your selection.

Life sciences       Behavioural & social sciences       Ecological, evolutionary & environmental sciences

For a reference copy of the document with all sections, see [nature.com/documents/nr-reporting-summary-flat.pdf](https://nature.com/documents/nr-reporting-summary-flat.pdf)

## Life sciences study design

All studies must disclose on these points even when the disclosure is negative.

Sample size	- Average vector fields (velocity and orientation) as well as the corresponding radial profiles were obtained by averaging at least 10 cellular disks per condition. Each cellular disk was imaged for at least 10 hours every 5 minutes, which correspond to a minimum of 120 timepoints per disk. - For fixed cellular disks we considered at least 10 disks to be sufficient for the statistical analyses. - The number of disks (N) used for each analyses is indicated in the main text and in the figure captions. - No temporal averaging was applied to the data prior to the calculation of errors.
Data exclusions	- Cellular islands with very low cell density did not feature collective behaviors and thus they were not considered for the analyses. - For averaging of orientational fields and calculation of related angles (psi and beta), only vectors with an associated anisotropy higher than a threshold (indicated in the figure captions) were considered.
Replication	- All the reported results were obtained from experiments repeated successfully and independently 2-3 times in different weeks. - Quantification always considered measurements from several cellular disks (N, indicated in the figure captions, see Sample Size).
Randomization	Samples (cellular disks) were randomly selected prior imaging.
Blinding	Blinding was not possible as the same researcher both obtained and analysed the data.

## Reporting for specific materials, systems and methods

We require information from authors about some types of materials, experimental systems and methods used in many studies. Here, indicate whether each material, system or method listed is relevant to your study. If you are not sure if a list item applies to your research, read the appropriate section before selecting a response.

Materials & experimental systems		Methods	
n/a	Involved in the study	n/a	Involved in the study
<input type="checkbox"/>	<input checked="" type="checkbox"/> Antibodies	<input checked="" type="checkbox"/>	<input type="checkbox"/> ChIP-seq
<input type="checkbox"/>	<input checked="" type="checkbox"/> Eukaryotic cell lines	<input checked="" type="checkbox"/>	<input type="checkbox"/> Flow cytometry
<input checked="" type="checkbox"/>	<input type="checkbox"/> Palaeontology and archaeology	<input checked="" type="checkbox"/>	<input type="checkbox"/> MRI-based neuroimaging
<input checked="" type="checkbox"/>	<input type="checkbox"/> Animals and other organisms		
<input checked="" type="checkbox"/>	<input type="checkbox"/> Human research participants		
<input checked="" type="checkbox"/>	<input type="checkbox"/> Clinical data		
<input checked="" type="checkbox"/>	<input type="checkbox"/> Dual use research of concern		

## Antibodies

Antibodies used	Myosin 4 Monoclonal Antibody (MF20), Alexa Fluor 488 (catalogue no., 53-6503-82, eBioscience, ThermoFischer)
Validation	This MF20 antibody has been reported for use in immunohistochemical staining, immunocytochemistry, and immunohistochemical staining of frozen tissue sections (see <a href="http://www.thermofisher.com/antibody/product/Myosin-4-Antibody-clone-MF20-Monoclonal/53-6503-82">www.thermofisher.com/antibody/product/Myosin-4-Antibody-clone-MF20-Monoclonal/53-6503-82</a> ).

## Eukaryotic cell lines

Policy information about <a href="#">cell lines</a>	
Cell line source(s)	Mouse C3H muscle myoblasts (C2C12, ECACC, catalogue no. 91031101)
Authentication	None of the cell lines have been authenticated.
Mycoplasma contamination	All cell lines tested negative for mycoplasma contamination.

Commonly misidentified lines  
(See [ICLAC](#) register)

No commonly misidentified cell lines were used.